Title: FHOD-1/profilin-mediated actin assembly protects sarcomeres against contraction-induced deformation in *C. elegans*

Authors: Michael J. Kimmich*[1], Sumana Sundaramurthy*[1], Meaghan A. Geary[1], Leila Lesanpezeshki[2], Curtis V. Yingling[1], Siva A. Vanapalli[2], Ryan S. Littlefield[3], David Pruyne[1,4]

[1] Department of Cell and Developmental Biology, State University of New York Upstate Medical University, Syracuse, NY 13210
[2] Department of Chemical Engineering, Texas Tech University, Lubbock, TX 79409
[3] Biology Department, University of South Alabama, Mobile, AL 36688
[4] Correspondence to pruyned@upstate.edu

* These authors contributed equally.

ABSTRACT
Formin HOmology Domain 2-containing (FHOD) proteins are a subfamily of actin-organizing formins that are important for proper striated muscle development in many animals. We had shown previously that absence of the sole FHOD protein, FHOD-1, in *C. elegans* results in thin body-wall muscles with misshapen dense bodies, structures that serve as sarcomere Z-lines in body-wall muscle. However, the mechanism of FHOD-1 action was unclear. Using mutations that target the actin assembly activity of FHOD-1, we demonstrate here that actin polymerization by FHOD-1 is required for its function in muscle development. Moreover, we show FHOD-1 cooperates with profilin PFN-3 to promote dense body morphogenesis, and profilins PFN-2 and PFN-3 to promote body-wall muscle growth. This is the first demonstration that a FHOD protein works with profilin partners in striated muscle development. Utilizing worms expressing fluorescently tagged dense body proteins PAT-3/β-integrin and ATN-1/α-actinin, we demonstrate dense bodies in *fhod-1* and *pfn-3* mutants are less stable than in wild type animals, having a higher proportion of dynamic protein, and becoming highly distorted by prolonged muscle contraction. We also observe the accumulation of actin depolymerization factor/cofilin homolog UNC-60B/cofilin in the body-wall muscle of these mutants. We suggest such accumulations may indicate targeting of thin filaments dislodged from unstable dense bodies disassembly. Similar failures in sarcomere assembly might account for the slow growth of body-wall muscle in *fhod-1* mutants compared to wild type animals, and the coincident muscle weakness that we measure in these animals. Overall, these results show the importance of FHOD protein-mediated actin assembly to forming stable sarcomere Z-lines, and identify profilin as a new contributor to FHOD activity in striated muscle development.

INTRODUCTION

Striated muscle across the animal kingdom is defined by a regularly repeating arrangement of well-ordered contractile units called sarcomeres, whose presence allows for rapid muscle contraction. The ends of sarcomeres, termed Z-lines, serve as sites where actin-based thin filaments are crosslinked and anchored in place, while the free ends of thin filaments project toward the sarcomere center to interdigitate with myosin-based thick filaments (Henderson et al.,

2017). During contraction, thick filaments pull the thin filaments so that the two filament types slide past each other, shortening the sarcomere (Huxley & Hanson, 1954).

Formin HOmology-2 Domain-containing (FHOD) proteins are a subgroup of actin-organizing formin proteins that have been implicated in proper striated muscle development in animals ranging from humans to nematodes. However, the contribution of FHOD homologs to sarcomere organization varies from organism to organism. Among mammals, FHOD3 is essential for sarcomere organization in cardiomyocytes. Rat- or human induced pluripotent stem cell-derived cultured cardiomyocytes are unable to assemble mature sarcomeres when FHOD3 is knocked down (Taniguchi et al., 2009; Iskratsch et al., 2010; Fenix et al., 2018). In mice deleted for the *fhod3* gene, cardiomyocytes make immature plasma membrane-associated sarcomeres, but these fail to mature and accumulate much lower levels of filamentous actin (F-actin) than in wild type mice (Kan-O et al., 2012). *Drosophila* indirect flight muscles (IFMs) also strongly depend on their sole FHOD homolog (called FHOS or FHOD), with FHOS knockout IFMs assembling less F-actin, and completely failing to organize these actin filaments into sarcomeres (Shwartz et al., 2016). Study of FHOS knockdown later in development in fly IFMs showed FHOD is also required to incorporate new thin filaments into growing sarcomeres, and to elongate the barbed ends of thin filaments already present in sarcomeres (Shwartz et al., 2016). In contrast to these examples, the striated body-wall muscle (BWM) of the simple nematode *Caenorhabditis elegans* is able to assemble sarcomeres even in absence of its sole FHOD homolog, FHOD-1. Worms lacking FHOD-1 assemble fewer sarcomeres per muscle cell, but these sarcomeres are functional and the ability of the worm to crawl or swim is not grossly affected (Mi-Mi et al., 2012; Mi-Mi & Pruyne, 2015). The formation of functional sarcomeres in these worms is not due to redundancy with any of the other five worm formins, as we have shown the formin CYK-1 affects BWM development through pleiotropic effects on overall body growth, while the remaining formins play no apparent role in BWM development (Mi-Mi et al., 2012; Sundaramurthy et al., 2020).

Formins are best known for their ability to stimulate actin filament assembly. Functioning as dimers, formins nucleate new actin filaments from monomers through their formin homolog-2 (FH2) domains, often in conjunction with additional actin-binding sites in the adjacent carboxy-terminal (C-terminal) extension or "tail" (Pruyne et al., 2002; Sagot et al., 2002; Gould et al., 2011; Vizcarra et al., 2014; Bremer et al., 2024). The ring-shaped FH2 dimer remains wrapped around the terminal actin subunits of the growing barbed end (Kovar & Pollard, 2004; Maufront et al., 2023). Depending on the formin, the effects of this can vary from blocking further actin incorporation ("tight capping") to allowing actin monomer incorporation at the barbed end without displacement of the formin ("processive capping") (Aydin et al., 2018). The formin homology-1 (FH1) domain contributes to actin assembly by binding the small actin monomer-binding protein, profilin, via FH1 domain poly-proline motifs, and transferring profilin-bound actin monomers to the FH2-bound barbed end (Kovar et al., 2003; Romero et al., 2004; Moseley et al., 2004). For many formins, including FHOD homologs, nucleation and processive capping depend on a universally conserved isoleucine of the FH2 domain (Xu et al., 2004; Patel et al., 2018; Antoku et al., 2019). For mammalian FHOD3, mutation of this isoleucine (I1127) to alanine prevents the formin from supporting sarcomere formation in cultured cardiomyocytes (Taniguchi et al., 2009), while overexpression of FHOD3(I1127A) in the mouse heart

recapitulates *fhod3* gene knockout phenotypes (Fujimoto et al., 2016). Similarly, *Drosophila* FHOD(I966A) is only partially functional, organizing actin filaments into small sarcomeres, but failing to support further sarcomere thickening or elongation (Shwartz et al., 2016). Thus, mammalian FHOD3 and *Drosophila* FHOS require their actin assembly activity in order to function properly in their respective muscles. Considering worm FHOD-1 is not required to assemble functional sarcomeres in BWM, we questioned whether worm FHOD-1 might function in a manner that does not depend on its actin assembly activity.

Here, we demonstrate that in fact actin polymerization by FHOD-1 is critical to proper BWM development in *C. elegans*. Moreover, we show that FHOD-1 works in conjunction with profilin, the first demonstration of formin/profilin cooperation in a striated muscle model. Finally, we show FHOD-1 and profilin are critical for ensuring resilient resiliency in the Z-line structures of BWM sarcomeres against severe deformation by the force of muscle contraction.

RESULTS

FHOD-1 defective for actin filament assembly activity does not support BWM growth or normal dense body morphogenesis.

The striated BWMs of *C. elegans* are strips of flat muscle cells that stretch from nose to tail. Each BWM cell is tightly adherent to a basement membrane shared with the overlying hypodermis (Waterston, 1988). F-actin- and myosin-rich sarcomeres are arranged in obliquely oriented striations that define the spindle shapes of these cells. Most BWM cells arise during embryogenesis, and grow through larval development and early adulthood, accumulating additional striations over time. We previously demonstrated the requirement for FHOD-1 for normal BWM growth through RNA interference (RNAi), or using deletion alleles *fhod-1(tm3138)*, predicted to eliminate a portion of the diaphanous inhibitory domain, and *fhod-1(tm2363)*, predicted to eliminate part of the FH2 domain and introduce a frameshift that prevents translation of downstream sequence (referred to here as *fhod-1(ΔFH2)*, Fig.1A) (Mi-Mi et al., 2012). That is, the spindle-shaped BWM cells in animals lacking *fhod-1* activity are narrower than those in wild type animals when measured at their widest point (Fig.1B, *solid arrows*), resulting in similarly narrow BWMs (Fig.1B, *dashed arrows*).

Expanding on our previous analysis (Mi-Mi et al., 2012), we confirmed BWM grows more slowly in larval and adult *fhod-1(ΔFH2)* animals compared to wild type, but observed these mutants proportionately narrow this size deficiency in older animals (Fig.1B-D). Examining the Z-line marker α-actinin (ATN-1 in *C. elegans*) to delineate the oblique striations of BWM cells, we observed that this slow growth of BWM cells in *fhod-1(ΔFH2)* animals correlates with a slower addition of new striations (Fig.1E,F). Additionally, as compared to wild type animals, more striations formed in *fhod-1(ΔFH2)* animals are misoriented, making fork-like intersections, a defect also observable when the central A band marker muscle myosin II heavy chain A/MYO-3 (Fig.1E,G-I). To test whether *fhod-1(ΔFH2)* also results in BWM weakness, we quantitatively measured force production using the NemaFlex platform, which calculates forces exerted by individual worms based on the degree to which they are able to deflect micropillars (Rahman et al., 2018). Consistent with their ~ 30% narrower BWMs, young adult *fhod-1(ΔFH2)* animals exert 29% less force, while by the third day of adulthood, *fhod-1(ΔFH2)* BWM is only 10%

narrower than wild type, and these animals apply a statistically insignificant 4% less force than wild type (Fig.1J). Thus, thinning of *fhod-1(ΔFH2)* BWM correlates well with muscle weakness.

To test the importance of the actin filament assembly activity of FHOD-1 in promoting BWM cell growth, we used CRISPR-Cas9 to introduce FH2 domain point mutations I904A and K1051A (Fig.1A). Both mutations target universally conserved actin-binding residues, with mutation of the isoleucine to alanine generally eliminating actin filament assembly activity in many formins, and mutation of the lysine to alanine typically having a milder effect (Xu et al., 2004; Ramabhadran et al., 2012). Immunoblot of whole worm extracts using an antibody raised against the FHOD-1 FH2 domain shows *fhod-1(I904A)* and *fhod-1(K1051A)* worms express FHOD-1 proteins at the correct predicted molecular weights (Fig.2A), including a higher molecular weight isoform we have shown previously is expressed in BWM (Refai et al., 2018). In contrast, extracts from *fhod-1(ΔFH2)* animals show only nonspecific immunoreactivity we have observed previously (Mi-Mi et al., 2012). Staining for F-actin showed that BWM cells in *fhod-1(I904A)* animals are narrower than wild type, but identical to BWM cells of age-matched *fhod-1(ΔFH2)* worms, and have nearly identically narrowed BWM cells with fewer striations than wild type (Fig.2B-D). In contrast, BWM cells of *fhod-1(K1051A)* were not significantly different from wild type (Fig.2B-D). Consistent with this, in tests for the ability of worms to burrow through 26% Pluronic gel (Lesanpezeshki et al., 2019), *fhod-1(ΔFH2)* and *fhod-1(I904A)* mutants perform worse than wild type animals to a very similar degree, while *fhod-1(K1051A)* worms are nearly as efficient as wild type animals (Fig.2E). Thus, the ability to assemble actin filaments appears critical for FHOD-1 function in promoting BWM cell growth and for normal BWM performance.

Another defect observed in *fhod-1(ΔFH2)* animals is malformation of their dense bodies. Dense bodies play two roles in BWM, serving as sarcomere Z-lines to anchor thin filaments, and as costameres to anchor sarcomeres to the plasma membrane (Gieseler et al., 2018). When viewed by immunostain for α-actinin/ATN-1, dense bodies are peg shaped structures arranged with fairly consistent spacing along striations in wild type animals (Sundaramurthy et al., 2020). We had shown previously that dense bodies in adult *fhod-1(ΔFH2)* mutants appear fragmented and irregular in shape, with irregular spacing along striations (Sundaramurthy et al., 2020). Immunostain for ATN-1 showed adult worms bearing *fhod-1(I904A)* also have irregular dense bodies identical to those of *fhod-1(ΔFH2)* animals, while dense bodies in *fhod-1(K1051A)* worms appear more regular in shape and spacing along striations, similar to those of wild type animals (Fig.2F). These data suggest FHOD-1 mediated actin assembly is essential for proper dense body morphology, with mutation of the conserved I904 having the greatest effect.

Profilin contributes to BWM cell growth and dense body formation similar to FHOD-1.

The *C. elegans* genome encodes three profilins: PFN-1, which is essential and expressed embryonically and in the adult nerve ring; PFN-2, which is non-essential and expressed primarily in pharyngeal muscle; and PFN-3, which is also non-essential and expressed primarily in BWM (Polet et al., 2006). Worms bearing the whole-gene deletion *pfn-3(tm1362)*, referred to here as *pfn-3(Δ)*, were reported to have no apparent phenotype, while RNAi against *pfn-2* in the *pfn-3(Δ)* background resulted in modestly misshapen dense bodies and sarcomeres that were slightly wider than in wild type worms (Polet et al., 2006). Additionally, *pfn-3(Δ)* worms performed

worse in Pluronic gel burrowing assays than wild type animals (Lesanpezeshki et al., 2021). To directly compare profilin- and *fhod-1*-deficient BWM, we stained F-actin in worms bearing *pfn-3(Δ)*, as well as worms bearing the whole-gene deletion *pfn-2(ok458)*, referred to here as *pfn-2(Δ)*, or animals deleted for both *pfn-2* and *pfn-3*. BWM cells of *pfn-2(Δ)* animals are nearly identical in size to age-matched wild type animals, while *pfn-3(Δ)* animals average one fewer striation per BWM cell compared to wild type, and double *pfn-2(Δ) pfn-3(Δ)* mutants have modestly narrower BWM cells and an average of two fewer striations per BWM cell (Fig.3A-F), effects similar to *fhod-1(ΔFH2)* but of lesser magnitude. Immunostain for ATN-1 revealed dense bodies are normal in *pfn-2(Δ)* animals, but somewhat irregular in shape and spacing in *pfn-3(Δ)* mutants or in double *pfn-2(Δ) pfn-3(Δ)* mutants, although often appearing not as irregular as in *fhod-1(ΔFH2)* animals (Fig.3G). Thus, PFN-3 and to a lesser extent PFN-2 contribute to BWM cell growth, and PFN-3 contributes to proper dense body morphogenesis, similar to FHOD-1.

To test whether the ability of the FHOD-1 FH1 domain to interact with profilin is important for muscle development, we used CRISPR-Cas9 to delete the three putative profilin-binding poly-proline stretches in the FH1 domain-coding sequence of *fhod-1* (Fig.1A). Immunoblotting verified *fhod-1(ΔFH1)* animals produce FHOD-1 protein of the expected molecular weights (Fig. 2A). By F-actin stain, BWM cells in *fhod-1(ΔFH1)* animals are smaller than those of wild type animals, with an identical width and striation number as age-matched double *pfn-2(Δ) pfn-3(Δ)* mutants (Fig.3D-F). And by immunostain for ATN-1, dense bodies in *fhod-1(FH1Δ)* animals are highly similar to those of *pfn-3(Δ)* mutants (Fig.4E). Thus, eliminating the predicted profilin-binding sites in the FHOD-1 FH1 domain has nearly identical effects on BWM development as elimination of PFN-2 and PFN-3.

To test whether profilins and FHOD-1 contribute to muscle development through a common mechanism or separate mechanisms, we examined BWM of animals mutated simultaneously for *fhod-1*, *pfn-2*, and *pfn-3*. We expected that if profilins contribute to BWM development strictly through FHOD-1-mediated actin filament assembly, the effect of these combined mutations should be no worse that the effect of eliminating only FHOD-1. Conversely, if profilins contribute to BWM development through additional FHOD-1-independent mechanisms, then the phenotype of triple mutants would exceed that of mutating *fhod-1* alone. Based on immunostain for ATN-1, dense bodies in triple *fhod-1(ΔFH1) pfn-2(Δ) pfn-3(Δ)* mutants appear similar to those of *fhod-1(ΔFH1)* or *pfn-3(Δ)* mutants (Fig.3G). Similarly, dense bodies in triple *fhod-1(ΔFH2) pfn-2(Δ) pfn-3(Δ)* appear similar to those of *fhod-1(ΔFH2)* mutants. These results suggest profilin, and particularly PFN-3, likely contributes to dense body morphogenesis through interaction with the FHOD-1 FH1 domain.

However, the effects of triple mutants on BWM cell growth were less straightforward. F-actin stain showed BWM cells of triple *fhod-1(ΔFH1) pfn-2(Δ) pfn-3(Δ)* mutants are narrower and have fewer striations than those of *fhod-1(FH1Δ)* or of double *pfn-2(Δ) pfn-3(Δ)* mutants (Fig.3D-F). Similarly, BWM growth was more reduced in triple *fhod-1(ΔFH2) pfn-2(Δ) pfn-3(Δ)* mutants than in *fhod-1(ΔFH2)* mutants (Fig.3A-C). These results suggest the profilins PFN-2 and PFN-3 make contributions to BWM cell growth independently of FHOD-1, although they may also contribute to BWM cell growth through FHOD-1-mediated actin filament assembly.

Dense bodies formed in absence of PFN-3 or FHOD-1 are unstable.

C. elegans dense bodies have a layered organization similar to focal adhesions, with a membrane-proximal zone with α-integrin/PAT-2 and β-integrin/PAT-3, an intermediate layer rich in vinculin/DEB-1, and an elongated segment rich in α-actinin/ATN-1 for thin filament attachment (Francis & Waterston, 1985; Barstead & Waterston, 1989; Gettner et al., 1995; Moulder et al., 2010). To better understand the effects of FHOD-1 on dense body dynamics, we examined animals expressing functional GFP-tagged β-integrin (GFP::PAT-3) and functional mCherry-tagged α-actinin (ATN-1::mCH) (Fig.4A,B, S1). As described previously, GFP::PAT-3 decorates all dense bodies, as well as M-lines and muscle cell-to-muscle cell adhesions called attachment plaques (Plenefisch et al., 2000). ATN-1::mCH also decorated most dense bodies, but was absent from small dense bodies at the ends of striations, at the edges of BWM cells (Fig.4A), a trait observed in wild type and *fhod-1(ΔFH2)* animals. However, ATN-1::mCH-positive dense bodies of *fhod-1(ΔFH2)* of all ages are more lobulated and variably shaped than in wild type worms (Figs 4B, S1), consistent with our previous ATN-1 immunostain of adult animals (Sundadarmurthy et al., 2020). Past analysis of dense body spacing in ATN-1-immunostained adults by fast Fourier transform (FFT) had shown wild type animals exhibit a semi-regular 1-µm spacing between dense bodies, while *fhod-1(ΔFH2)* animals have no preferred spacing (Sundaramurthy et al., 2020). Consistent with and expanding upon this, FFT analysis of dense bodies in ATN-1::mCH-expressing animals showed wild type animals exhibit regular spacing throughout growth, trending from ~ 0.7 µm between dense bodies in the youngest stage-1 larvae (L1) to > 1.8 µm at the fourth day of adulthood (Table 1, Figs S2, S3). Conversely, FFT analysis of *fhod-1(ΔFH2)* dense bodies shows no preferred spacing through larval development, and only weak and inconsistent preferred spacing in older *fhod-1(ΔFH2)* adults (Table 1, Figs S2, S3). Thus, dense body malformation appears to be present throughout development.

To test whether protein dynamics in *fhod-1(ΔFH2)* dense bodies are abnormal, we performed fluorescence recovery after photobleaching (FRAP). Individual dense bodies were photobleached in immobilized L4 larvae and monitored for recovery for 40 or 72 min (Fig.4C,D). GFP::PAT-3 showed a slow, linear recovery of fluorescence that did not saturate, and did not differ between wild type and *fhod-1(ΔFH2)* animals (Fig.4C,D). ATN-1::mCH recovered more rapidly in wild type and *fhod-1(ΔFH2)* animals, with *fhod-1(ΔFH2)* dense bodies showing a greater degree of fluorescence recovery (Fig.4C,D), suggesting the α-actinin-rich portion of dense bodies that anchors thin filaments is more dynamic in absence of FHOD-1. We reasoned that if dense bodies were defective in anchoring thin filaments in *fhod-1(ΔFH2)* animals, we might observe enhanced recruitment of the muscle-specific actin depolymerization factor (ADF)/cofilin homolog, UNC-60B, a protein essential for actin filament turnover in BWM (Ono et al., 1999). In wild type animals, we observed UNC-60B in low amounts along the Z-lines (Fig.5), as shown previously (Ono et al., 1999). However, in *fhod-1(ΔFH2)* animals, UNC-60B also accumulates at the pointed ends of BWM cells (Fig.5, *arrows*). We had not previously noted F-actin accumulation at BWM cell ends in *fhod-1(ΔFH2)* animals, but ADF/cofilin and phalloidin bind competitively to actin filaments (Nishida et al., 1987; Ono et al., 1996; Ono & Ono, 2009). Probing for actin by immunostain showed UNC-60B at the *fhod-1(ΔFH2)* BWM cell ends overlaps with actin (Fig.5, *arrows*). We observed similar but fainter UNC-60B accumulation at BWM cell ends in double *pfn-2(Δ) pfn-3(Δ)* mutants, with faint overlapping

actin immunostain (Fig.5). Distinct from *fhod-1(ΔFH2)* animals, profilin mutants also accumulate UNC-60B puncta in the BWM cytoplasm outside the layer of sarcomeres (Fig.5, *arrowheads in Organellar Layer*), consistent with profilins playing at least some FHOD-1-independent roles in BWM cell development.

Based on our evidence that the thin filament-binding portion of dense bodies in *fhod-1(ΔFH2)* mutants is more dynamic than in wild type, we hypothesized that the deformed shape of *fhod-1(ΔFH2)* dense bodies might arise from an inability to resist pulling forces during muscle contraction. To test this, worms were grown on a bacterial lawn containing 2.5 mM levamisole, a nicotinic acetylcholine receptor agonist. This maintained BWMs in a partially contracted state, as verified by a tauter appearance of the animals, although the worms were still able to crawl. After 24 h treatment, 100% wild type and 95% *fhod-1(ΔFH2)* levamisole-treated worms remained alive. Where sarcomeres in wild type BWM are largely unaffected by this treatment, sarcomeres of levamisole-treated *fhod-1(ΔFH2)* animals are highly distorted compared to untreated controls (Fig.6A). Dense bodies in treated *fhod-1(ΔFH2)* animals, as viewed through ATN-1::mCH and PAT-3::GFP, are stretched to form nearly continuous-appearing Z-lines rather than discontinuous bodies (Fig.6A, *arrows*), and striations are contorted rather than straight. There is also an increased presence of diffuse PAT-3::GFP across the BWM cell membrane in levamisole-treated *fhod-1(ΔFH2)* muscle, while M-line-associated PAT-3::GFP is reduced (Fig.6A). We also tested whether prolonged muscle relaxation reversed dense body morphological defects by growing *fhod-1(ΔFH2)* worms on a bacterial lawn containing 10 mM muscimol, a γ-aminobutyric acid receptor agonist. However, this treatment did not dramatically improve *fhod-1(ΔFH2)* dense bodies, suggesting deformation of dense bodies may be irreversible (Fig.6A).

As a quantitative measure of the effects of levamisole treatment on dense bodies, we immunostained control- or levamisole-treated worms for ATN-1, and measured the percent surface area taken up by the dense body marker in two-dimensional projections of the sarcomeres (Fig.6B,C). By this metric, wild type animals exhibit very modest dense body deformation resulting ATN-1 occupying 2.4% more of the total area after levamisole treatment. Dense body deformation was quantitatively greater in *fhod-1(ΔFH2)* mutants, with ATN-1 occupying 5% more of the total area (Fig.6B,C). Similarly, dense bodies in *pfn-3(Δ)* mutants occupy 4.7% greater area, and those in double *pfn-2(Δ) pfn-3(Δ)* occupy 3.9% greater area (Fig.6B,C), supporting a common FHOD-1/profilin pathway for dense body morphogenesis.

Considering FHOD-1 is important for the ability of dense bodies to resist prolonged muscle contraction, we tested whether FHOD-1 is actively recruited to dense bodies during levamisole treatment. Under normal conditions, a functional GFP-tagged FHOD-1 (FHOD-1::GFP) localizes to small bodies along the lateral edges of BWM cells (Fig.7, *white arrows*), and fainter bodies within sarcomeres, particularly around and between dense bodies (Fig.7, *cyan arrows*). This is consistent with the localization of endogenous FHOD-1 (Mi-Mi et al., 2012). Localized FHOD-1::GFP remains visible through larval development and young adulthood, but fades to nearly undetectable by the third day of adulthood when BWM cell growth has ceased (Fig.7, *L4* versus *Day 3 Adult*). Interestingly, in levamisole-treated wild type animals, FHOD-1::GFP is largely absent from BWMs (Fig.7, *control* versus *levamisole*), consistent with our observation that BWM cells in levamisole-treated animals grow noticeably less during treatment than those of controls. Notably, this result suggests FHOD-1 is not recruited to strengthen dense

bodies during prolonged contraction. Instead, we suggest stability is established in dense bodies in a FHOD-1-dependent manner during their formation.

DISCUSSION

In vivo cooperation between FHOD-1 and profilin in striated muscle development

We had shown previously that among six members of the formin family of actin organizing proteins in *C. elegans*, only FHOD-1 directly contributes to the development of the body-wall muscle (BWM) in a cell autonomous manner (Mi-Mi et al., 2012; Sundaramurthy et al., 2020). In absence of FHOD-1, BWM cells add new striations more slowly during development, resulting in slower BWM growth (Fig.1E,F). Additionally, dense bodies, which serve as sarcomere Z-lines, are misshapen and irregular in shape and spacing when formed in absence of FHOD-1 (Figs 4A, S1). However, unlike mouse and fly models for FHOD-dependent muscle development, sarcomeres of FHOD-1-deficient BWMs are functional, and contain abundant actin-based thin filaments (Mi-Mi & Pruyne, 2015). This led to the question of whether FHOD-1 functions independently of the ability to stimulate the actin filament polymerization. We show here that a *fhod-1* mutant bearing the FH2 domain point mutation I904A predicted disrupt actin filament assembly phenocopies a functionally null *fhod-1* allele for BWM cell growth, dense body morphology, and muscle performance in burrowing assays (Fig.2). A second FH2 point mutation K1051A predicted to have milder impact on actin filament assembly had little observable effect on these phenotypes.

Many formins have been shown to work with the actin monomer-binding protein profilin *in vivo* to promote actin filament assembly, using the FH1 domain to recruit profilin with bound actin to the growing ends of elongating actin filaments (Coutemanche, 2018). We provide here the first *in vivo* demonstration of cooperation between a FHOD homolog and profilin in straited muscle development. Absence of the profilin PFN-3, which is primarily expressed in BWM (Polet et al., 2006), results in similar dense body morphological defects as seen in *fhod-1* mutants, and particularly animals mutated to lack the FHOD-1 FH1 domain (Fig.3G). Moreover, we saw no additive effects on dense bodies with simultaneous loss of PFN-3 and the FHOD-1 FH1 domain, suggesting PFN-3 and the FHOD-1 FH1 domain cooperate to promote dense body morphogenesis (Fig.3G).

These results differ slightly from Polet and colleagues, who noted dense body morphology defects only when both PFN-3 and a second profilin, PFN-2, were perturbed (Polet et al., 2006). One possible explanation for this discrepancy is that that study probed dense body morphology through observation of vinculin/DEB-1, which occupies a relatively smaller proportion of the dense body than does α-actinin/ATN-1 (Barstead & Waterston, 1989; Moulder et al., 2010), making observation of small morphological changes challenging. Additionally, our FRAP analysis suggests the α-actinin-rich portion of dense bodies may be particularly sensitive to loss of FHOD-1/profilin activity (Fig.4C,D). However, their results may indicate PFN-2 also contributes to dense body morphogenesis, although to a lesser degree than PFN-3.

We did observe PFN-2 contributes to BWM cell growth redundantly with PFN-3. Thus, worms lacking PFN-3 have only very modest BWM cell growth defects, but worms lacking both PFN-2 and PFN-3 have greater defects (Fig.3A-C). However, combined absence of PFN-2, PFN-

3, and FHOD-1 results in BWM growth defects even greater than those caused by absence of profilins or FHOD-1 alone, indicating the profilins must make FHOD-1-independent contributions to BWM growth (Fig.3A-C). Considering profilins also mediate ATP/ADP-nucleotide exchange for actin, suppress pointed end elongation of actin filaments, and interact with other proteins, this result is not surprising (Pimm et al., 2020). Perhaps related to this, we noted worms doubly mutated for *pfn-2* and *pfn-3* accumulate small puncta of ADF/cofilin/UNC-60B in their cytoplasm (Fig.5), possibly indicating a wider disturbance in cytoskeletal organization in the BWM cell. Alternatively, PFN-2 is predominantly expressed in the pharyngeal muscle that is required for feeding (Polet et al., 2006), so that some of the effects of that profilin on BWM growth might be secondary to overall reduced growth, consistent with our observation that worms triply mutated for *fhod-1*, *pfn-2*, and *pfn-3* are smaller than age-matched single or double mutant counterparts.

Cooperation between FHOD homologs and profilin has not been demonstrated *in vivo* in other striated muscle systems, but we believe this is likely to be a conserved mechanism. Supporting this, normal sarcomere growth in indirect flight muscles (IFMs) of *Drosophila* requires its FHOD homolog FHOS to be competent to assemble actin filaments (Shwartz et al., 2016), and FHOS cooperates with profilin *in vitro* to promote actin filament assembly (Patel et al., 2018). There is also indirect supporting evidence from studies with cultured rat cardiomyocytes showing hyperactivation of FHOD3 or overexpression of profilin-1 is each sufficient to induce hypertrophy (Kooij et al., 2016; Zhou et al., 2017). Additionally, in humans, autosomal dominant mutations in *fhod3* cause between 1-2% of inherited cases of hypertrophic cardiomyopathy (HCM) (Ochoa et al., 2018), and expression of FHOD3 is elevated in the HCM heart in humans (Wooten et al., 2013), while mouse models of HCM show elevated profilin-1 expression (Kooij et al., 2016). Based on these and on our results, we suggest it is likely FHOD3 and profilin function as partners in promoting cardiomyocyte hypertrophy, analogous to how FHOD-1 and profilin promote BWM cell growth in the worm.

FHOD-1 and profilin impart stability onto dense bodies.

When viewed by electron microscopy, dense bodies in wild type animals appear as solid electron-dense structures, but in *fhod-1(ΔFH2)* mutants appear partially fragmented (Mi-Mi & Pruyne, 2015). Considering thin filaments are anchored to dense bodies, we hypothesized this partial fragmentation of dense bodies in *fhod-1(ΔFH2)* animals might result from the pulling forces of muscle contraction on thin filaments, with *fhod-1(ΔFH2)* dense bodies being physically less stable than those of wild type animals. We show here by several metrics that dense bodies are less stable in worms lacking functional FHOD-1 or PFN-3, and this particularly affects the α-actinin-rich portion where thin filaments are anchored. Confirming that muscle contraction is a deforming force, dense bodies in BWM of *fhod-1* and *pfn-3* mutants become highly distorted during prolonged pharmacologically induced contraction (Fig.6). Even under normal conditions, a higher proportion of α-actinin in dense bodies is exchangeable with the cytoplasm in *fhod-1(ΔFH2)* mutant BWM cells (Fig.4C,D), suggesting less of the substance of the dense body is firmly anchored in place. Possibly related, *fhod-1* and *pfn-3* mutant BWM cells also accumulate ADF/cofilin at BWM cell ends (Fig.5). An intriguing hypothesis is that these accumulations

represent regions where thin filaments dislodged from dense bodies have accumulated and been targeted for depolymerization.

Despite our evidence FHOD-1 and PFN-3 cooperate *in vivo*, the distribution of the two proteins in BWM cells differ. Previous immunostain for PFN-3 shows this profilin isoform concentrates at the tips of dense bodies in BWM cells (Polet et al., 2016). In contrast, FHOD-1 is found in small bodies distinct from dense bodies along BWM cell edges, as well as in small amounts around and between dense bodies (Fig.7) (Mi-Mi et al., 2012). Interestingly, we also observe incomplete dense bodies lacking ATN-1 at BWM cell edges (Fig.4A), which may indicate these are immature dense bodies that formed most recently in the BWM cell. FHOD-1 does not colocalize with these dense bodies, but their proximity might indicate FHOD-1-generated actin filaments might affect them during to their formation. Similarly, the presence of FHOD-1 near dense bodies deeper in the muscle cell may support their continued development, as dense bodies continue to grow in size through larval development and early adulthood (Figs 4B, S1) (Moerman & Williams, 2006). However, it is unlikely FHOD-1 actively maintains dense body integrity after dense bodies have finished assembling, as after BWM cell growth ceases, FHOD-1 is no longer localized near dense bodies (Fig.7, *L4* versus *Day 3 Adult*). Additionally, FHOD-1 is not recruited to dense bodies during prolonged muscle contraction, when dense bodies are subject to deforming forces (Fig.7). As yet, it is unclear exactly how FHOD-1/PFN-3-mediated actin filament assembly strengthens dense bodies. One model is FHOD-1 and PFN-3 might elongate thin filament barbed ends sufficiently to ensure the filaments are firmly embedded through the full mass of the dense body. Alternatively, FHOD-1/PFN-3 might polymerize an as-yet unidentified population of nonsarcomeric actin filaments that plays a supporting role for dense bodies, analogous to the role that intermediate filaments play in bridging Z-discs in vertebrate striated muscles (Henderson et al., 2017).

We suggest the small BWM sizes of *fhod-1* and *pfn-3* mutants are secondary consequences of dense body fragility. As sarcomeres form and enlarge during BWM growth, we suggest subsets of thin filaments in *fhod-1* and *pfn-3* mutants become dislodged and are disassembled. A base rate of sarcomere assembly failure might also explain our previous observation that muscle myosin II heavy chain/MYO-3 is subject to elevated levels of proteasome-driven proteolysis in *fhod-1(ΔFH2)* BWM (Yingling & Pruyne, 2021). However, a net productive sarcomere assembly permits formation of new striations at a slowed rate, resulting in narrow muscle (Figs 1J, 2E). With all other factors remaining equal, we expect muscle strength to be proportional to cross-sectional area (Moss et al., 1997). BWM cells in *fhod-1(ΔFH2)* adults have the same length as wild type animals, and the same radial thickness when viewed in cross sections (Mi-Mi et al., 2012). Thus, the degree of lateral narrowing in BWM correlates directly with changes in cross-sectional area. In line with this, the measured muscle weakness observed in *fhod-1(ΔFH2)* animals correlates very well with their width of their BWM relative to wild type animals (Fig.1J).

In several ways, the relationship between FHOD-1 and dense bodies resembles the relationship between FHOD3 and sarcomeres in the mouse heart. During heart development in the mouse, cardiomyocytes assemble immature sarcomeres that organize into stress fiber-like premyofibrils that support an early heartbeat (Kan-O et al., 2012). Normally, sarcomeres in premyofibrils mature by forming proper Z-lines and incorporating additional thin filaments, but

in *fhod3* knockout cardiomyocytes, sarcomeric organization is lost, and α-actinin- and F-actin-rich aggregates form (Kan-O et al., 2012). An intriguing possibility is that in the absence of FHOD3, nascent cardiomyocyte sarcomeres are unstable, similar to *fhod-1* mutant dense bodies. The mouse heart begins beating as premyofibrils are forming in the mouse heart, leaving open the possibility that sarcomeres in the *fhod3* knockout become disrupted by the increasing contractile forces of the developing heart. It would be interesting to test whether modest reductions in contractility would support more advanced sarcomere assembly in *fhod3*-deficienty cardiomyocytes. Another parallel between worm FHOD-1 and mouse FHOD3 is that neither seems strictly required to maintain sarcomeres after they have assembled. Thus, after conditional knockout of FHOD3 from the adult mouse heart, sarcomeres are maintained and the heart becomes mildly enlarged (Ushijima et al., 2018). These commonalities may suggest that despite the difference in the magnitude of their phenotypes, the loss of these conserved proteins in worm and mouse may have very similar mechanistic consequences on sarcomeric organization.

MATERIALS AND METHODS

Worms strains and growth conditions

Worms were grown on nematode growth medium (NGM) plates with OP50-1 *Escherichia coli* bacterial food at 20˚C following standard protocols (Brenner, 1974). Where needed, worms were age-synchronized by dissolving gravid adults in 1:2 ratio reagent grade bleach:5 M NaOH to liberate embryos (Bartel, 1991), and hatching embryos into L1 larvae overnight at 20˚C in M9 buffer (Ausubel et al., 2002). To induce prolonged partial muscle contraction or relaxation (for Figs 6,7), OP50-1 culture was mixed with 2.5 mM levamisole, 10 mM muscimol, or no drug (control) prior to seeding 500 µl to 60-mm NGM plates, or 250 µl to 35-mm NGM plates, similar to as described (Brouilly et al., 2018). L4 stage larvae were washed once with M9 buffer and added to dried plates for 24 h treatment at 20˚C.

All worm strains used in this study are listed in Table 2. Worm strain DWP294 (genotype *rhIs2[pat-3::HA::gfp]*) was previously created (Plenefisch et al., 2000) but was not previously named. CRISPR-Cas9-mediated mutagenesis was performed on worms by injecting the syncytial gonad with Cas9 protein (Integrated DNA Technologies, IDT, Coralville, IA), tracrRNA (IDT), gene-specific crRNAs (IDT), and single-stranded oligodeoxynucleodites (ssODNs) (IDT) for homology-directed repair, as described (Paix et al., 2015). Allele *fhod-1(ups176)*, encoding amino acid change I904A and a novel *MwoI* cut site for PCR-based genotyping, was generated using crRNA [UUU AGU UAG ACC AAU GUU GAG UUU UAG AGC UAU GCU] and ssODN [AAA CTC TAT CTG TTC TTC CTC TGA AAA GAT CGC AAG CAA TCA ACG CAG GTC TAA CTA AAT TGC CAC CGA TCA ACG TCA TCC CTG CAG CAA TTA T]. Allele *fhod-1(ups177)*, encoding K1051A and eliminating an endogenous *BamHI* site, was generated with crRNA [AAC AAA AGC AUC AGA AGU AAG UUU UAG AGC UAU GCU] and ssODN [GGA ACT GAT ATT AAG GGT TTC TAT CTG GAT TAT TTA ACA AAA GCA TCA GAA GTA GCA GAT CCA GTC TAC AAG CAT ACT TTG ACA TAT CAC]. Allele *fhod-1(ups185)*, encoding a deletion of G768 to G805 of the FH1 domain, was generated with crRNAs [CGU GGA GGU CCU GGU GUG UUU UAG AGC UAU GCU] and [AUU CCU CCA CCU CCU CCU CCG UUU UAG AGC UAU GCU], and ssODN [CGG AGA ATG GAA

TGC GTG GAG GTC CTG TTG GTG TTA ATT TGC TTA TGA ACG GTA TAA ATC GAG GAG ATA T]. All CRISPR-generated *fhod-1* alleles were verified by sequencing the modified loci, and were outcrossed six times to a clean N2 (wild type) background. All amino acid residue numbers are relative to FHOD-1 isoform A, as currently defined on WormBase http://www.wormbase.org/db/get?name=CE41309#06--10;class=protein.

For visualization of α-actinin in live animals, RSL62 was generated by CRISPR-Cas9 mediated homology directed repair (Dickenson et al., 2013) using a co-conversion strategy (Arribere et al., 2014). Briefly, the repair plasmid was generated in two steps: blunt-end cloning of N2 genomic DNA to isolate upstream and downstream homology arms, followed by isothermal assembly to incorporate the bicistronic tagging cassette consisting of *linker-mCherry::ICR::GFP-nls* in-frame at the 3' end of the *atn-1* coding sequence. The trans-splicing ICR was derived from operon CEOP1032. The *GFP* and *mCherry* sequences were respectively derived from pJA245 and pJA281, which were gifts from Julie Ahringer (Addgene plasmids #21506 and #22513) (Zeiser et al., 2011). The Cas9 sgRNA plasmid was generated according to Arribere and colleagues (2014) using pRB1017, a gift from Andrew Fire (Addgene plasmid #59936). For further details on targeting of *atn-1* with Cas9, see Supplemental Methods. The RSL62 strain was outcrossed five times with wildtype N2 worms without any noticeable change in fluorescence.

Western blot analysis

Worms were collected and lysed after washing from plates, as previously described (Yingling & Pruyne, 2021). Sample loads for western blot analysis were normalized based on Coomassie brilliant blue stain of extracts after SDS-PAGE. Normalized extract samples were resolved by SDS-PAGE followed by transfer to nitrocellulose for probing with polyclonal antibody DPMSP2 (affinity-purified anti-FHOD-1 FH2 domain; Mi-Mi et al., 2012) diluted 1:200 in 1% milk/Tris-buffered saline, pH 8.3 (Fig.2A).

Fixation and staining for fluorescence microscopy

Fixation and stain for F-actin with Alexa Fluor 568-phalloidin was as previously (Mi-Mi et al., 2012). Fixation and immunostain was as previously (Finney & Ruvkun, 1990), but with omission of spermidine-HCl and an increased methanol concentration (75%) during fixation. Monoclonal antibody MH35 (anti-ATN-1) developed by R.H. Waterston (Francis & Waterston, 1985) was a generous gift from P. Hoppe (Western Michigan University, Kalamazoo, MI). Monoclonal antibody 5-6-s (anti-MYO-3) developed by H.F. Epstein (Miller et al., 1983) was obtained through the Developmental Studies Hybridoma Bank, created by the NICHD of the NIH and maintained at The University of Iowa, Department of Biology, Iowa City, IA 52242. Polyclonal anti-UNC-60B (Ono & Ono, 2002) was a gift from S. Ono (Emory University, Atlanta, GA). Monoclonal antibody clone C4 (anti-actin) is commercially available (Thermo Fisher Scientific, Waltham, MA). Primary antibody dilutions were MH35 $1:10^4$, 5-6-s $1:10^3$, anti-UNC-70B 1:200, DPMSP2 1:200, and C4 1:50. Secondary antibodies Texas red-conjugated goat anti-rabbit and fluorescein isothiocyanate-conjugated goat-anti-mouse (Rockland Immunochemicals, Limerick, PA) were diluted 1:500.

Fluorescence microscopy and image analysis

Wide-field fluorescence images (Fig.1H) were acquired using an Eclipse 90i upright microscope (Nikon, Tokyo, Japan) with a CFI Plan Apochromat 40X/NA 1.0 oil immersion objective or CFI Plan Apochromat violet corrected 60X/NA 1.4 oil immersion objective with a Cool-SNAP HA2 digital monochrome charge-coupled device camera (Photometrics, Tucson, AZ) at room temperature, driven by NIS-Elements AR acquisition and analysis software (version 3.1; Nikon). Confocal images (all other figure images) were acquired using an SP8 Laser Scanning Confocal Microscope (Leica, Wetzlar, Germany) driven by LAS X Software (version 3.5.2, build 4758; Leica), and using an HCX Plan Apochromat 63X/NA 1.4 oil immersion lambda objective. Confocal z-stacks of BWMs were collected at 0.1 µm intervals (Figs 1B,E, 4A,B, 6A, 7) or 0.3 µm intervals (Figs 2F, 3G, 5, 6B) before deconvolution using Huygens Essential software (Huygens compute engine 18.10.0, Scientific Volume Imaging B.V.), Classic Maximum Likelihood Estimation deconvolution algorithm, with 40 iterations and a signal/noise ratio of 20. Maximum intensity projections (MIPs) were generated from deconvolved confocal z-stacks using LAS X software or ImageJ (version 2.0.0-rc-65/1.51 g) (Schneider et al., 2012). Images were linearly processed to enhance contrast and false colored in Adobe Photoshop CS4 or CC2018 (Adobe, San Jose, CA). Deconvolved confocal z-stacks were also used to construct 3D renderings (Figs 4B, S1) using Imaris x64 software (version 9.2.1; Bitplane AG, Belfast, United Kingdom).

Measuring of BWM widths and muscle cell widths, and counting of striations per BWM cell were all performed on BWM cells positioned within four to five cells of the vulva to ensure consistency in size, as BWM cells taper in width toward the head and tail. For results shown in Fig,1C, D, F, and G, four BWM cells in ten animals of each genotype and age were analyzed, in each of two independent replicates. For results shown in 2B-D and 3A-F, two to four BWM cells in 20 animals of each genotype were analyzed in each of three independent replicates. BWM and BWM cell widths were measured and striations per BWM cells were counted on phalloidin-stained worms (Figs 1C,D, 2B-D, 3A-F), as previously (Sundaramurthy et al., 2020). In young larvae, it is difficult to unambiguously identify BWM striations based on F-actin stain. Therefore, ATN-1::mCH-positive dense bodies were used to identify striations for counting in BWM cells across multiple ages (Fig.1F). Non-parallel striations, identified as those that intersect other striations, were also counted in these cells (Fig.1G). The prevalence of non-parallel striations was also quantified by acquiring single focal plane images of MYO-3 immunostain in six wild type and 13 *fhod-1(ΔFH2)* worms, counting all non-parallel striations in all intact BWM cells, and measuring the combined length of all visible MYO-3 striations in those cells. The prevalence of non-parallel striations was expressed as the number of occurrences per 10,000 µm of striation measured in each image (Fig.1I).

FFT analyses on ATN-1::mCH fluorescence intensity profiles (Table 1, Figs S2, S3) were performed as previously for ATN-1 immunostain (Sundaramurthy et al., 2020). Fluorescence profiles were measured over eight dense body-containing striations in one muscle cell (or all striations in two muscle cells for L1 larvae) in each of ten animals per strain and per developmental stage. To quantify the effects of 24 h levamisole treatment on dense body morphology (Fig.6C), confocal images showing four to five BWM cell striations were acquired from 15 ATN-1 immunostained worms per genotype per condition, in each of three independent

replicates. Images were deconvolved as above, and maximum intensity projections were processed through a macro that set a binary threshold of grey values 20-255 to generously mask ATN-1 signal with minimal background, and analyzed particles as % Area. This assay was performed three times. All quantitative measures were performed while blinded to strain genotype.

FRAP analysis

For analysis of dense body protein dynamics in live animals (Fig.4C,D), L4 stage larvae were immobilized in 3.5 µl polystyrene nanobead suspension (2.5% by volume, 0.1 µm diameter; Polysciences, Warrington, PA) sandwiched between a coverslip and a 10% agarose pad. Worms were viewed for PAT-3::GFP or ATN-1::mCH fluorescence on an SP8 Laser Scanning Confocal Microscope, as above. For each of four (for PAT-3::GFP FRAP) or five (for ATN-1::mCH FRAP) worms of each genotype tested, four regions of interest (ROIs), each encompassing one dense body were photobleached twice under the FRAP application with 100% laser power, and subsequently imaged for 40 min (for PAT-3::GFP) or 72 min (for ATN-1::mCH). Animals were confirmed to be alive at the end of each experiment. Fluorescence analysis was conducted in ImageJ, measuring at each time point (t) maximum fluorescence intensity values in same-sized ROIs surrounding the four experimental photobleached dense bodies (F_{exp}) and two control unbleached dense bodies (F_{unb}), as well as mean fluorescence intensity values for same-sized ROIs surrounding three background areas of BWM with no dense bodies or other PAT-3::GFP/ATN-1::mCH-containing structures ($\bar{F}_{back}$). Percent fluorescence was calculated as: $(100 * (F_{exp}^{t} - \bar{F}_{back}^{t}) * (F_{unb}^{0} - \bar{F}_{back}^{0})) / ((F_{exp}^{0} - \bar{F}_{back}^{0}) * (F_{unb}^{t} - \bar{F}_{back}^{t}))$.

Pluronic gel burrowing assay

Worms at one day of adulthood were analyzed for the ability to burrow through 26% (w/v) pluronic F-127 (Sigma-Aldrich, St. Louis, MO) gel (Fig.2E), as previously described (Lesanpezeshki et al., 2019). Every 10 min, worms that had burrowed successfully through 0.76 cm gel to chemoattractant OP50-1 on the surface were counted. This assay was performed four times on 30 worms per genotype per replicate.

Muscle strength measurements using the Nemaflex platform

Strength measurements were conducted using the NemaFlex platform (Fig.1J) as previously described (Rahman et al.., 2018). Briefly, at least 30 animals were loaded individually into polydimethylsiloxane microfluidic chambers filled with M9 buffer, where they crawled between free-end deflectable micropillars with diameter, gap, and height of 44 µm, 71 µm, and 87 µm, respectively. Animals were imaged for 1 min at 5 fps at 20 ± 1˚C using a Ti-E microscope (Nikon) with an Andor Zyla sCMOS 5.5 camera (Oxford Instruments, Abingdon, United Kingdom). Movies were analyzed using a custom-built image processing software (MATLAB, R2016a; https://github.com/VanapalliLabs/NemaFlex). Muscle strength was calculated based on the maximum pillar deflection identified in each frame, using the Timoshenko theory for an elastic rod (Timoshenko & Gere, 1972). The maximum exerted force f_{95} was calculated as the 95th percentile of all maximal deflections for each animal and reported as muscle strength by averaging over the population tested.

Statistical analysis

Data are expressed as average ± standard deviation, except Fig.1J reporting average ± SEM. Graphs were made in Excel:Windows (version 21H1; Microsoft Corporation, Redmond, WA) or Prism 10 (version 10.1.1; GraphPad Software, Boston, MA). For muscle strength measurements, statistical analysis was performed using a Wilcoxon rank-sum test. For other experiments, where two groups were compared, data were analyzed using a student t-test, and where three or more groups were compared, data were analyzed using a one-way analysis of variation, followed by Tukey's multiple comparisons *post hoc* test. $p \leq 0.05$ was considered statistically significant.

ACKNOWLEDGMENTS

Some worm strains were provided by the CGC, which is funded by NIH Office of Research Infrastructure Programs (P40 OD010440). We thank Peter Calvert for help with FFT analysis, and WormBase and WormBook. R.S.L. would like to thank Anna Lee McKinney for assistance in the generation of RSL62. This work was supported by the Francis Hendricks Endowment Fund (to D.P.), University of South Alabama Research Development Award (to R.S.L.), a National Science Foundation EPSCoR Research Infrastructure Improvement Track 4 Grant (Award #1738564 to R.S.L.), and the National Aeronautics and Space Administration (NNX15AL16G to S.A.V.).

REFERENCES

Antoku S, Wu W, Joseph LC, Morrow JP, Worman HJ, Gundersen GG (2019). ERK1/2 phosphorylation of FHOD connects signaling and nuclear positioning alternations in cardiac laminopathy. *Dev Cell* 51, 602-616.

Arribere JA, Bell RT, Fu BXH, Artiles KL, Hartman PS, Fire AZ (2014). Efficient marker-free recovery of custom genetic modifications with CRISPR/Cas9 in *Caenorhabditis elegans*. *Genetics* 193, 837--846.

Ausubel FM, Brent R, Kingston RE, Moore DD, Seidman JG, Smith JA, Struhl K (1992). Short Protocols in Molecular Biology 2nd Edition, New York: Willey.

Aydin F, Courtemanche N, Pollard TD, Voth GA (2018). Gating mechanisms during actin filament elongation by formins. *Elife* 7, e37342.

Barstead RJ, Waterston RH (1989). The basal component of the nematode dense-body in vinculin. *J Biol Chem* 264, 10177-10185.

Bremer KV, Wu C, Patel AA, He KL, Grunfeld AM, Chanfreau GF, Quinlan ME (2024). Formin tails act as a switch, inhibiting or enhancing processive actin elongation.

Brenner S (1974). The genetics of *Caenorhabditis elegans, Genetics* 77, 71-94.

Brouilly N, Lecroisey C, Martin E, Pierson L, Mariol M-C, Qadota H, Labouesse M, Streichenberger N, Mounier N, Gieseler K (2015). Ultra-structural time-course study in the *C. elegans* model for Duchenne muscular dystrophy highlights a crucial role for sarcomere-anchoring structures and sarcolemma integrity in the earliest steps of the muscle degeneration process. *Hum Mol Genet* 24, 6428-6445.

Courtemanche N (2018). Mechanisms of formin-mediated actin assembly and dynamics. *Biophys Rev* 10, 1553-1569.

Dickinson DJ, Ward JD, Reiner DJ, Goldstein B (2013) Engineering the *Caenorhabditis elegans* genome using Cas9-triggered homologous recombination. *Nat Methods* 10, 1028-1034.

Fenix AM, Neininger AC, Taneja N, Hyde K, Visetsouk MR, Garde RJ, Liu B, Nixon BR, Manalo AE, Becker JR, et al. (2018). Muscle-specific stress fibers give rise to sarcomeres in cardiomyocytes. *Elife* 7, e42144.

Finney M, Ruvkun G (1990). The *unc-86* gene product couples cell lineage and cell identity in *C. elegans*. *Cell* 63, 895-905.

Francis GR, Waterston RH (1985). Muscle organization in *Caenorhabditis elegans*: localization of proteins implicated in thin filament attachment and I-band organization. *J Cell Biol* 101, 1532-1549.

Fujimoto N, Kan-O M, Ushimima T, Kage Y, Tominaga R, Sumimoto H, Takeya R (2016). Transgenic expression of the formin protein Fhod3 selectively in the embryonic heart: role of actin-binding activity of Fhod3 and its sarcomeric localization during myofibrillogenesis. *PLoS One* 11, e0148472.

Gettner SN, Kenyon C, Reichardt LF (1995). Characterization of bpat-3 heterodimers, a family of essential integrin receptors in *C. elegans. J Cell Biol* 129, 1127-1141.

Gieseler K, Qadota H, Benian GM (2017). Development, structure, and maintenance of *C. elegans* body wall muscle. In: Wormbook, ed. The *C. elegans* Research Community, doi/10.1895/wormbook.1.81.

Gould CJ, Maiti S, Michelot A, Graziano BR, Blanchoin L, Goode BL (2011). The formin DAD domain plays dual roles in autoinhibition and actin nucleation. *Curr Biol* 21, 384-390.

Iskratsch T, Lange S, Dwyer J, Kho AL, dos Remedios C, Ehler E (2010). Formin follows function: a muscle-specific isoform of FHOD3 is regulated by CK2 phosphorylation and promotes myofibril maintenance. *J Cell Biol* 191, 1159-1172.

Henderson HA, Gomez CG, Novak SM, Mi-Mi L, Gregorio CC (2017). Overview of the muscle cytoskeleton. *Compr Pysiol* 7, 891-944.

Huxley H, Hanson J (1954). Changes in the cross-striations of muscle during contraction and stretch and their interpretation. *Nature* 173, 973-976.

Kan-O M, Takeya R, Abe T, Kitajima N, Nishida M, Tominaga R, Kurose H, Sumimoto H (2012). Mammalian formin Fhod3 plays an essential role in cardiogenesis by organizing myofibrillogenesis. *Biol Open* 1, 889-896.

Kooij V, Viswanathan MC, Lee DI, Rainer PP, Schmidt W, Kronert WA, Harding SE, Kass DA, Bernstein SI, Van Eyk JE, et al. (2016). Profilin modulates sarcomeric organization and mediates cardiomyocyte hypertrophy. *Cardiovasc Res* 110, 238-248.

Kovar DR, Kuhn JR, Tichy AL, Pollard TD (2003). The fission yeast cytokinesis formin Cdc12p is a barbed end actin filament capping protein gated by profilin. *J Cell Biol* 161, 875-887.

Kovar DR, Pollard TD (2004). Insertional assembly of actin filament barbed ends in association with formins produces piconewton forces. *Proc Natl Acad Sci U S A* 101, 14725-14730.

Maufront J, Guichard B, Cao-L-Y, Di Cicco A, Jégou A, Romet-Lemonne G, Bertin A (2023). Direct observation of the conformational states of formin mDia1 at actin filament barbed ends and along the filament. *Mol Biol Cell* 34, ar2.

Miller DM, III, Ortiz I, Berliner GC, Epstein HF (1983). Differential localization of two myosins within nematode thick filaments. *Cell* 34, 477-490.

Moerman DG, Williams BD (2006). Sarcomere assembly in *C. elegans* muscle. In: Wormbook, ed. The *C. elegans* Research Community, doi/10.1895/wormbook.1.81.

Moulder GL, Cremona GH, Juerr J, Stirman JN, Fields SD, Martin W, Qadota H, Benian GM, Lu H, Barstead RJ (2010). a-actinin is required for the proper assembly of Z-disk/focal-

adhesion-like structures and for efficient locomotion in *Caenorhabditis elegans*. *J Mol Biol* 403, 516-528.
Lesanpezeshki L, Hewitt JE, Laranjeiro R, Antebi A, Driscoll M, Szewczyk NJ, Blawzdziewicz J, Lacerda CMR, Vanapalli SA (2019). Pluronic gel-based burrowing assay for rapid assessment of neuromuscular health in *C. elegans. Sci Rep* 9, 15246.
Lesanpezeshki L, Qadota H, Darabad MN, Kashyap K, Lacerda CMR, Szewczyk NJ, Benian GM, Vanapalli SA (2021). Investigating the correlation of muscle function tests and sarcomere organization in *C. elegans*. *Skelet Muscle* 11, 20.
Mi-Mi L, Votra S, Kemphues K, Bretscher A, Pruyne D (2012). Z-line formins promote contractile lattice growth and maintenance in striated muscles of *C. elegans. J Cell Biol* 198, 87-102.
Mi-Mi L, Pruyne D (2015). Loss of sarcomere-associated formins disrupts Z-line organization, but does not prevent thin filament assembly in *Caenorhabditis elegans* muscle. *J Cytol Histol* 6, 318.
Moseley JB, Sagot I, Manning AL, Xu Y, Eck MJ, Pellman D, Goode BL (2004). A conserved mechanism of Bni1- and mDia1-induced actin assembly and dual regulation of Bni1 by Bud6 and profilin. *Mol Biol Cell* 15, 896-907.
Moss BM, Refsnes PE, Abildgaard A, Nicolaysen K, Jensen J (1997). Effects of maximal effort strength training with different loads on dynamic strength, cross-sectional area, load-power and load-velocity relationships. *Eur J Appl Physiol* 75, 193-199.
Nishida E, Iida K, Yonezawa N, Koyasu S, Yahara I, Sakai H (1987). Cofilin is a component of intranuclear and cytoplasmic actin rods induced in cultured cells. *Proc Natl Acad Sci U S A* 84, 5262-5266.
Ochoa JP, Sabater-Molina M, García-Pinilla JM, Morgensen J, Restrepo-Córdoba A, Palomino-Doza J, Villacorta E, Martinez-Moreno M, Ramos-Maqueda J, Zorio E, et al. (2018) Formin homology 2 domain containing 3 (FHOD3) is a genetic basis for hypertrophic cardiomyopathy. *J Am Coll Cardiol* 72, 2457-2467.
Ono K, Ono S (2002). Tropomyosin inhibits ADF/cofilin-dependent actin filament dynamics. *J Cell Biol* 156, 1065-1076.
Ono K, Ono S (2009). Actin-ADF/cofilin rod formation in *Caenorhabditis elegans* muscle requires a putative F-actin binding site of ADF/cofilin at the C-terminus. *Cell Motil Cytoskeleton* 66, 398-408.
Ono S, Abe H, Obinata T (1996). Stimulus-dependent disorganization of actin filaments induced by overexpression of cofilin in C2 myoblasts. *Cell Struct Funct* 21, 491-499.
Ono S, Baillie DL, Benian GM (1999). UNC-60B, an ADF/cofilin family protein, is required for proper assembly of actin into myofibrils in *Caenorhabditis elegans* body wall muscle. *J Cell Biol* 145, 491-502.
Paix A, Folkmann A, Rasoloson D, Seydoux G (2015). High efficiency, homology-directed genome editing in *Caenorhabditis elegans* using CRISPR-Cas9 ribonucleoprotein complexes. *Genetics* 201, 47-54.
Patel AA, Oztug Durer ZA, van Loon AP, Bremer KV, Quinlan ME (2018). *Drosophila* and human FHOD family formin proteins nucleate actin filaments. *J Biol Chem* 293, 532-540.
Pimm ML, Hotaling J, Henty-Ridilla JL (2020). Profilin choreographs actin and microtubules in cells and cancer. *Int Rev Cell Mol Biol* 355, 155-204.

Plenefisch JD, Zhu X, Hedgecock EM (2000). Fragile skeletal muscle attachments in dystophic mutants of *Caenorhabditis elegans*: isolation and characterization of the *mua* genes. *Development* 127, 1197-1207.

Polet D, Lambrechts A, Ono K, Mah A, Peelman F, Vandekerckhove J, Baillie DL, Ampe C, Ono S (2006). *Caenorhabditis elegans* expresses three functional profilins in a tissue-specific manner. *Cell Motil Cytoskeleton* 63, 14-28.

Pruyne D, Evangelista M, Yang C, Bi E, Zigmond S, Bretscher A, Boone C (2002). Role for formins in actin assembly: nucleation and barbed-end association. *Science* 297, 612-615.

Rahman M, Hewitt JE, Van-Bussel F, Edwards H, Blawzdziewicz J, Szewczyk NJ, Driscoll M, Vanapalli SA (2018). NemaFlex: a microfluidics-based technology for standardized measurements of muscular strength of *C. elegans. Lab Chip* 18, 2187-2201.

Ramabhadran V, Gurel PX, Higgs HN (2012). Mutations to the formin homology 2 domain of INF2 protein have unexpected effects on actin polymerization and severing. *J Biol Chem* 287, 34234-34245.

Refai O, Smit RB, Votra S, Pruyne D, Mains PE (2018). Tissue-specific functions of *fem-2*/PP2c phosphatase and *fhod-1*/formin during *Caenorhabditis elegans* embryonic morphogenesis. *G3 (Bethesda)* 8, 2277-2290.

Romero S, Le Clainche C, Didry D, Egile C, Pantaloni D, Carlier M-F (2004). Formin is a processive motor that requires profilin to accelerate actin assembly and associated ATP hydrolysis. *Cell* 119, 419-429.

Sagot I, Rodal AA, Moseley J, Goode BL, Pellman D (2002). An actin nucleation mechanism mediated by Bni1 and profilin. *Nat Cell Biol* 4, 626-631.

Schneider CA, Rasband WS, Eliceri KW (2012). NIH image to ImageJ: 25 years of image analysis. *Nature Methods* 9, 671-675.

Shwartz A, Dhanyasi N, Schejter ED, Shilo B-Z (2016). The *Drosophila* formin Fhos is a primary mediator of sarcomeric thin-filament array assembly. *Elife* 5, e16540.

Sundaramurthy S, Votra S, Laszlo A, Davies T, Pruyne D (2020). FHOD-1 is the only formin in *Caenorhabditis elegans* that promotes striated muscle growth and Z-line organization in a cell autonomous manner. *Cytoskeleton (Hoboken)* 77, 422-441.

Taniguchi K, Takeya R, Suetsugu S, Kan-O M, Narusawa M, Shoise A, Tominaga R, Sumimoto H (2009). Mammalian formin fhod3 regulates actin assembly and sarcomere organization in striated muscles. *J Biol Chem* 284, 29873-29881.

Timoshenko S, Gere JM (1971). Mechanics of Materials, New York: Van Nostrand Reinhold Company.

Ushijima T, Fujimoto N, Matsuyama S, Kan-O M, Kiyonari H, Shioi G, Kage Y, Yamasaki S, Takeya R, Sumimoto H (2018). The actin-organizing formin protein Fhod3 is required for postnatal development and functional maintenance of the adult heart in mice. *J Biol Chem* 293, 148-162.

Vizcarra CL, Bor B, Quinlan ME (2014). The role of formin tails in actin nucleation, processive elongation, and filament bundling. *J Biol Chem* 289, 30602-30613.

Xu Y, Moseley JB, Sagot I, Poy F, Pellman D, Goode BL, Eck MJ (2004). Crystal structures of a formin homology-2 domain reveal a tethered dimer architecture. *Cell* 116, 711-723.

Waterston RH (1988). Muscle. In: The Nematode *Caenorhabditis elegans*, ed. W. B. Wood, New York: Cold Spring Harbor Laboratory Press, 281-335.

Wooten EC, Hebl VB, Wolf MJ, Greytak SR, Orr NM, Draper I, Calvino JE, Kapur NK, Maron MS, Kullo IJ, et al. (2013) Formin homology 2 domain containing 3 variants associated with hypertrophic cardiomyopathy. *Circ Cardiovasc Genet* 6, 10-18.

Yingling CV, Pruyne D (2021). FHOD formin and SRF promote post-embryonic striated muscle growth through separate pathways in *C. elegans*. *Exp Cell Res* 398, 112388.

Zeiser E, Frøkjær-Jensen C, Jorgensen E, Ahringer J (2011). MosSCI and gateway compatible plasmid toolkit for constitutive and inducible expression of transgenes in the *C. elegans* germline. *PLoS One* 6, e20082.

Zhou Q, Wei S-S, Wang H, Wang Q, Li W, Li G, Hou J-W, Chen X-M, Chen J, Xu W-P, et al. (2017). Crucial role of ROCK2-mediated phosphorylation and upregulation of FHOD3 in the pathogenesis of angiotensin II-induced cardiac hypertrophy. *Hypertension* 69, 1070-1083.

Table 1. Dense body spacing along striations.

Age	Predominant Dense Body Spacing[†]	
	Wild Type	*fhod-1(ΔFH2)*
L1	0.73 µm, n/a[‡]	n/a[‡], n/a[‡]
L4	1.17 µm, 1.45 µm	n/a[‡], n/a[‡]
Day 1 Adult	1.50 µm, 2.38 µm	n/a[‡], 2.00 µm
Day 3 Adult	1.58 µm, 2.09 µm	3.74 µm, n/a[‡]
Day 4 Adult	1.84 µm, 2.25 µm	2.64 µm, n/a[‡]

[†] Values shown are calculated as the inverse of the primary frequency (μm^{-1}) determined by FFT analysis of ATN-1::mCH fluorescence along striations (Figs S1, S2). Values from each of two trials are shown, determined from fluorescence profiles of all dense body-containing striations of two muscle cells (for L1 larvae) or eight dense body-containing striations in one muscle cell (for other ages) in each of ten animals per strain per developmental stage.

[‡] No primary frequency was present, or the calculated predominant dense body spacing spanned multiple dense bodies.

Table 2. Worm strains used in this study.

Strain	Genotype	Source[†]	Figure(s)
DWP3	*qaIs8001[fhod-1::GFP mini-unc-119(+)]*	Mi-Mi et al., 2012	Parental stain
DWP229	*atn-1(ftw35) V; rhIs2[pat-3::HA::GFP]*	RSL62, DWP294	1E-G, 4A-D, 6A, S1, S2, S3
DWP230	*fhod-1(tm2363) I; atn-1(ftw35) V; rhIs2[pat-3::HA::GFP]*	XA8001, DWP229	1E-G, 4B-D, 6A, S1, S2, S3
DWP231	*atn-1(ftw35 atn-1::mCH::ICR::GFPnls] V; rhIs2[pat-3::HA::GFP]; qaIs[fhod-1::GFP mini-unc-119(+)]*	DWP3, RSL62	7
DWP284	*pfn-3(tm1362) X*	N2 outcross of ON167	3A-C,G, 6B,C
DWP285	*fhod-1(ups175 [I904A]) I*	CRISPR N2	2A-F
DWP286	*fhod-1(ups180 [K1051A]) I*	CRISPR N2	2A-F
DWP287	*pfn-2(ok458) X*	N2 outcross of RB694	3A-C,G
DWP292	*pfn-3(tm1362) pfn-2(ok458) X*	DWP284, DWP287	3A-G, 6B,C
DWP294	*rhIs2[pat-3::HA::GFP]*	Plenefisch et al., 2000	Parental strain
DWP296	*fhod-1(tm2363) I; pfn-3(tm1362) pfn-2(ok458) X*	XA8001, DWP292	3A-C,G
DWP303	*fhod-1(ups185 [ΔFH1]) I*	CRISPR N2	3D-G
DWP314	*fhod-1(ups185) I; pfn-3(tm1362) pfn-2(ok458) X*	DWP292, DWP303	3D-G
N2	Bristol wild type	CGC[‡]	1B-D, H-J, 2A-F, 3A-G, 5, 6B,C
ON167	*pfn-3(tm1362) X*	CGC[‡]	Parental strain
RB694	*pfn-2(ok458) X*	CGC[‡]	Parental strain
RSL62	*atn-1(ftw35 [atn-1::mCH::ICR::GFPnls]) V*	Ryan Littlefield	Parental strain
XA8001	*fhod-1(tm2363 [ΔFH2]) I*	Mi-Mi et al., 2012	1B-D, H-J, 2A-F, 3A-G, 5, 6B, C

[†]Reference for initial isolation of strain, or parental strains for strains produced in this study.

[‡]*Caenorhabditis* Genetic Center (University of Minnesota, Minneapolis, MN)

FIGURE LEGENDS

Figure 1. FHOD-1 is required for normal and timely formation of striations during BWM cell growth. (A) Predicted effects of point mutations (*black arrowheads*) or deletions (*black bars*) in mutants used in this study relative to FHOD-1 structural domains GTPase-binding domain (GBD), diaphanous inhibitory domain (DID), formin homology-1 domain (FH1), formin homology-2 domain (FH2), and two predicted diaphanous autoregulatory domains (*dark red bars*). Numbers indicate amino acid residues of FHOD-1 isoform A. **(B)** Maximum intensity projections of deconvolved confocal z-stacks showing BWMs in dorsal views of phalloidin-stained animals, showing examples of the widths of BWMs (*dashed arrows*) and of individual muscle cells (*solid arrows*). Scale bars, 6 µm. **(C)** BWM widths and **(D)** mucle cell widths were measured for phalloidin-stained worms of larval stages L1 and L4, and animals after one day of adulthood (A1), three days (A3), or four days (A4) (n = 10 animals per genotype per age per trial, 4 BWMs or 4 mucle cells per animal, in two independent trials). Growth of muscle cells in *fhod-1(ΔFH2)* animals lag behind those of wild types. **(E)** Maximum intensity projections of deconvolved confocal z-stacks showing BWMs in dorsal views of animals expressing ATN-1::mCH dense body marker. Intersecting non-parallel striations are more commonly observed in *fhod-1(ΔFH2)* animals (*arrows*) than in wild type animals (*arrowheads*). Scale bars, 6 µm. **(F)** Numbers of ANT-1::mCH-marked striations per muscle cell and **(G)** numbers of non-parallel ANT-1::mCH-marked striations per muscle cell were counted for indicated ages and genotypes (n = 10 animals per genotype per age per trial, 4 BWM cells per animal, in two independent trials). Muscle cells in *fhod-1(ΔFH2)* animals add new striations slower than wild type animals, but accumulate more non-parallel striations. **(H)** Wide-field dorsal views of worms immunostained for MYO-3 show that intersections between non-parallel striations (*arrowheads*) are more prevalent in *fhod-1(ΔFH2)* animals. Scale bars, 50 µm. **(I)** Shown are numbers of non-parallel MYO-3 striations counted per combined measured length of MYO-3 striations visible in wide-field views (n = 6 wild type or 13 *fhod-1(ΔFH2)* worms in one trial). **(J)** Muscle strengths of young (day 0) adults and day 3 adults were measured using the Nemaflex platform. Young adult *fhod-1(ΔFH2)* animals are weaker than wild types, but come close to matching wild type animal strength by the third day of adulthood. Numerical results shown as individual measures and averages ± standard deviation, except **J** showing mean ± SEM. (*) $p < 0.05$; (**) $p < 0.01$; (***) $p < 0.001$; (ns, not significant) $p > 0.05$.

Figure 2. FHOD-1-stimulated actin filament polymerization is required for BWM growth and dense body morphogenesis. (A) Two anti-FHOD-1 immunoblots of whole worm extracts reveal previously described ~150 kDa and ~165 kDa FHOD-1 isoforms in animals bearing point mutations *fhod-1(I904A)* and *fhod-1(K1051A)* and deletion mutation *fhod-1(ΔFH1)*, but not bearing the deletion and frameshift mutation *fhod-1(ΔFH2)*. Previously observed nonspecific immunoreactivity to lower molecular weight proteins is visible for all strains. **(B)** BWM widths and **(C)** widths of individual muscle cells were measured, and **(D)** numbers of striations per muscle cell were counted in phalloidin-stained day 1 adults (n = 20 animals per genotype per trial, two to four BWMs or muscle cells per animal, in three independent trials), showing muscle cells of *fhod-1(I904A)* animals are nearly identically to those of *fhod-1(ΔFH2)* mutants, while *fhod-1(K1051A)* muscle cells are nearly wild type. Numerical results shown as individual measures and averages ± standard deviation. All comparisons are statistically significant, $p < 0.001$, except those indicated (ns, not significant, $p > 0.05$). **(E)** Fraction of day 1 adult worms

able to successfully burrow through 26% pluronic gel was determined every 10 min for 1 h (n = 30 worms per genotype per trial, in four independent trials). Results shown as averages ± standard deviation. No differences were statistically significant owing to large trial-to-trial differences, but *fhod-1(I904A)* and *fhod-1(ΔFH2)* animals consistently perform poorly compared to wild type and *fhod-1(K1051A)* animals in each assay. **(F)** Maximum intensity projections of confocal z-stacks show dorsal views of day 1 adults immunostained for dense body marker ATN-1. Dense bodies appear regular in shape and spacing in wild type animals, but irregular in shape and spacing in *fhod-1(ΔFH2)* and *fhod-1(I904A)* mutants. Dense bodies in *fhod-1(K1051A)* animals are very similar to those in wild type animals. Scale bar, 5 µm.

Figure 3. Profilins and FHOD-1 FH1 domain are required for normal BWM cell growth and dense body morphogenesis. (A-C) Comparison of single and double profilin mutants to *fhod-1(ΔFH2)* mutants for **(A)** BWM width, **(B)** widths of individual muscle cells, and **(C)** numbers of striations per muscle cell, in day 1 adults (n = 20 animals per genotype per trial, two to four BWMs or muscle cells per animal, in three independent trials). Loss of the profilin genes *pfn-2* and *pfn-3* contribute to all three BWM metrics, although their combined effects are less than that of *fhod-1(ΔFH2)*. **(D-F)** Comparison of single and double profilin mutants to *fhod-1(ΔFH1)* mutants for **(D)** BWM width, **(E)** widths of individual muscle cells, and **(F)** numbers of striations per muscle cell, in day 1 adults (n = 20 animals per genotype per trial, two to four BWMs or muscle cells per animal, in three independent trials). The effects of the loss of profilin genes *pfn-2* and *pfn-3* on BWM metrics closely match the effects of *fhod-1(ΔFH1)*. Results shown as individual measures and averages ± standard deviation. All comparisons are statistically significant, $p < 0.001$, except those indicated (ns, not significant, $p > 0.05$). **(F)** Maximum intensity projections of confocal z-stacks show dorsal views of day 1 adults immunostained for dense body marker ATN-1. Dense bodies appear similarly irregular in *pfn-3(Δ)* mutants, double *pfn-2(Δ) pfn-3(Δ)* mutants, and *fhod-1(ΔFH1)* mutants. Scale bar, 5 µm.

Figure 4. α-actinin is more mobile in dense bodies formed in the absence of FHOD-1. (A) Maximum intensity projection of a deconvolved confocal z-stack of a day 1 adult expressing PAT-3::GFP and ATN-1::mCH. Both markers are associated with dense bodies, although dense body composition varies along striations, starting as small dense bodies at striation ends (DB1) with PAT-3::GFP only, and becoming progressively larger (DB2 to DB3) and associated with ATN-1::mCH. PAT-3::GFP is also associated with M-lines (M) and attachment plaques (A), which can be identified based on their differing morphologies. Scale bar, 10 µm. **(B)** Three-dimensional reconstructions from deconvolved confocal z-stacks show dense bodies from PAT-3::GFP/ATN-1::mCH-expressing adults. PAT-3::GFP is present at the plasma membrane and ATN-1::mCH is present in elongated projections embedded in the sarcomere lattice. Dense bodies tend to be shorter and wider in *fhod-1(ΔFH2)* animals. Scale bars, 1 µm. **(C)** Single confocal images of live L4 larvae show PAT-3::GFP- or ATN-1::mCH-marked dense bodies prior to bleaching, immediately after bleaching targeted dense bodies, and after 24 min of recovery. Scale bars, 5 µm. **(D)** Quantification of fluorescence recovery of photobleached dense bodies in images similar to **C** (for PAT-3::GFP, n = 4 worms of each genotype, 4 dense bodies per animal; for ATN-1::mCH, n = 5 worms of each genotype, 4 dense bodies per animal). PAT-3::GFP recovers slowly and to similar degrees in wild type and *fhod-1(ΔFH2)* animals, while ATN-1::mCH recovers more rapidly in both strains, but to a greater degree in *fhod-1(ΔFH2)* animals.

Results shown are averages ± standard deviation. (*) $p < 0.05$. No differences were significant between wild type and *fhod-1(ΔFH2)* animals at any time point for PAT-3::GFP ($p > 0.05$).

Figure 5. BWM cells lacking FHOD-1 or PFN-3 accumulate ADF/cofilin-associated actin filaments. Maximum intensity projections of deconvolved confocal z-stacks show day 1 adults immunostained for actin and UNC-60B. UNC-60B and actin are organized into striations in BWM. In *fhod-1(ΔFH2)* animals, and to a lesser extent in *pfn-2(Δ) pfn-3(Δ)* animals, UNC-60B also accumulates at the pointed ends of muscle cells (*arrows*). Additionally, *pfn-2(Δ) pfn-3(Δ)* animals accumulate small puncta of UNC-60B (*arrowheads*) in the portion of the muscle cell cytoplasm occupied by organelles, below the layer of sarcomeres. Scale bar, 5 µm.

Figure 6. Dense bodies formed in absence of FHOD-1 or PFN-2/PFN-3 are highly deformed by prolonged contraction. (A) Maximum intensity projections of deconvolved confocal z-stacks show day 1 adults expressing PAT-3::GFP and ATN-1::mCH. Dense bodies in wild type animals were largely unaffected after 24 h treatment with 2.5 mM levamisole, which stimulates muscle contraction, or with 10 µM muscimol, which inhibits muscle contraction. In contrast, dense bodies in *fhod-1(ΔFH2)* animals were highly distorted by levamisole treatment, forming nearly continuous stripes of dense body material (*arrows*). Scale bars, 6 µm. **(B)** Maximum intensity projections of deconvolved confocal z-stacks show day 1 adults immunostained for ATN-1. Scale bar, 2 µm. **(C)** Levamisole treatment more strongly distorts dense bodies in *fhod-1(Δ), pfn-3(Δ),* and double *pfn-2(Δ) pfn-3(Δ)* mutants than in wild-type animals, as quantified by the total area occupied by ATN-1 in maximum intensity projections in untreated (-) and levamisole-rteated (+) animals (n = 1 image from each of 15 worms per genotype per condition per trial, with three independent trials). All were significantly changed by levamisole treatment ($p < 0.001$), although effects on mutants were of greater magnitude than on wild type worms.

Figure 7. FHOD-1 is present among sarcomeres during BWM growth, but not under conditions of prolonged contraction. Maximum intensity projections of deconvolved confocal z-stacks show dorsal views of animals expressing FHOD-1::GFP and ATN-1::mCH. In L4 larvae, FHOD-1 is present in bodies along the edges of BWM cells (*white arrows*), and in faint striations (*cyan arrows*) that intersect dense bodies. By day 3 adulthood, most localized FHOD-1::GFP is gone. Treatment of day 1 adults with levamisole for 24 h results in delocalization of FHOD-1::GFP, as compared to untreated controls. Scale bars, 10 µm.

SUPPLEMENTARY FIGURE LEGENDS

Figure S1. Three-dimensional reconstructions from deconvolved confocal z-stacks show BWM from PAT-3::GFP/ATN-1::mCH-expressing animals. Dense bodies at ends of striations frequently contain PAT-3::GFP only (*cyan arrowheads*), while dense bodies away from the striation ends have ATN-1::mCH-rich projections (*white arrows*). PAT-3::GFP is also present in M-lines (*white arrowheads*). Dense bodies in *fhod-1(ΔFH2)* animals are short, wide, and sometimes lobulated (*cyan arrows*) compared to wild type. Scale bars, 1 µm.

Figure S2. Loss of FHOD-1 disrupts dense body spacing in all ages of animals. Maximum intensity projections of deconvolved confocal z-stacks show ATN-1::mCH-expressing larvae and adults. Scale bars, 4 µm. Dense body spacing along striations was analyzed by performing FFT

analysis on ATN-1::mCH fluorescence intensity profiles from images such as these (n = 10 animals per strains per developmental stage, 8 dense body-containing striations from 1 BWM cell or 2 BWM cells for L1 larvae, data shown for first of two trials).

Figure S3. Loss of FHOD-1 disrupts dense body spacing in all ages of animals. Maximum intensity projections of deconvolved confocal z-stacks show ATN-1::mCH-expressing larvae and adults. Scale bars, 4 µm. Dense body spacing along striations was analyzed by performing FFT analysis on ATN-1::mCH fluorescence intensity profiles from images such as these (n = 10 animals per strains per developmental stage, 8 dense body-containing striations from 1 BWM cell or 2 BWM cells for L1 larvae, data shown for second of two trials).

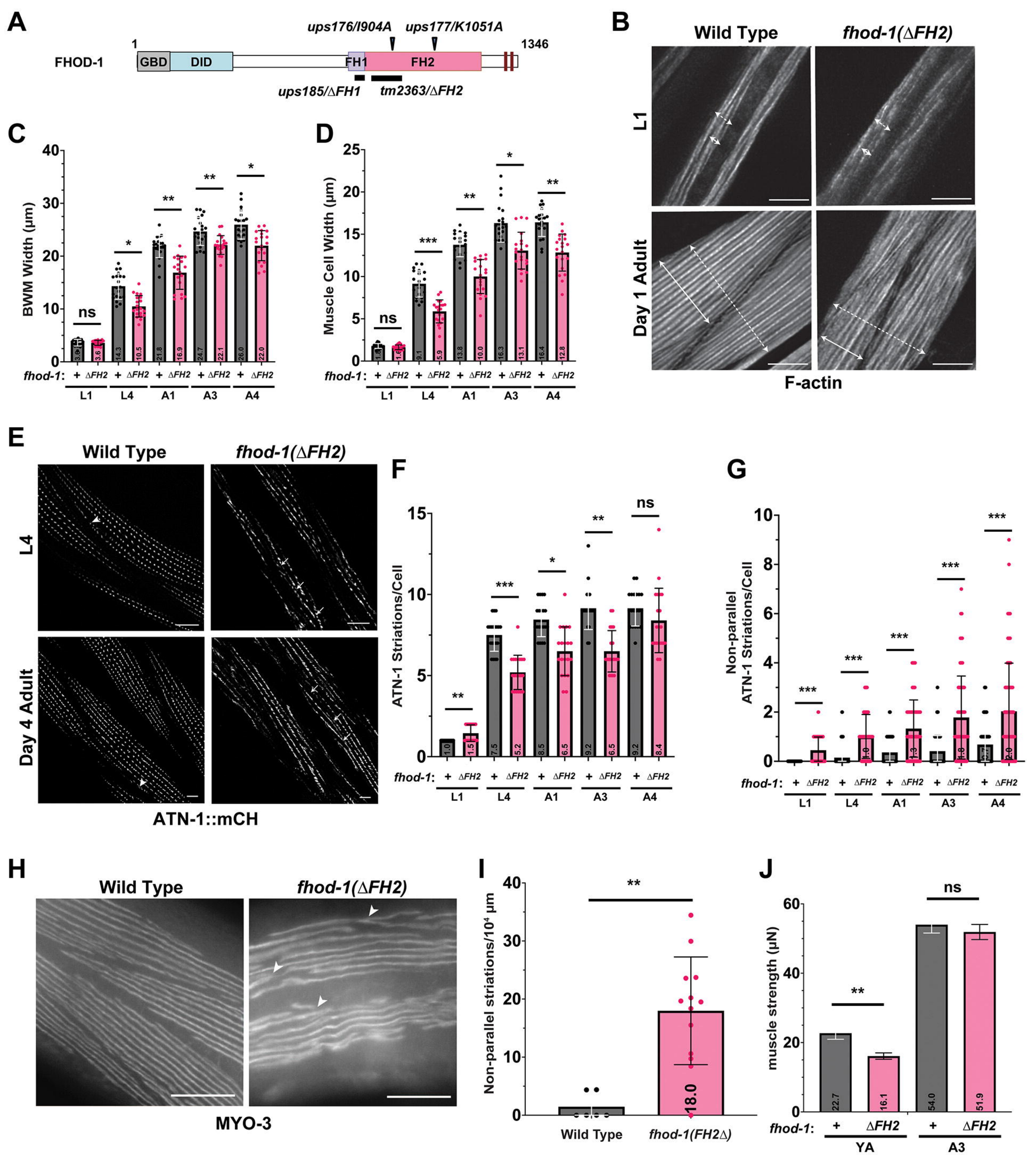
A
ups176/I904A
ups177/K1051A
1
1346
FHOD-1
GBD
DID
FH1
FH2
ups185/ΔFH1
tm2363/ΔFH2
B
Wild Type
fhod-1(ΔFH2)
L1
Day 1 Adult
F-actin
C
BWM Width (µm)
fhod-1: + ΔFH2 + ΔFH2 + ΔFH2 + ΔFH2 + ΔFH2
L1 L4 A1 A3 A4
D
Muscle Cell Width (µm)
E
L4
Day 4 Adult
ATN-1::mCH
F
ATN-1 Striations/Cell
G
Non-parallel ATN-1 Striations/Cell
H
MYO-3
I
Non-parallel striations/10⁴ µm
Wild Type
fhod-1(FH2Δ)
J
muscle strength (µN)
YA
A3

Figure 1

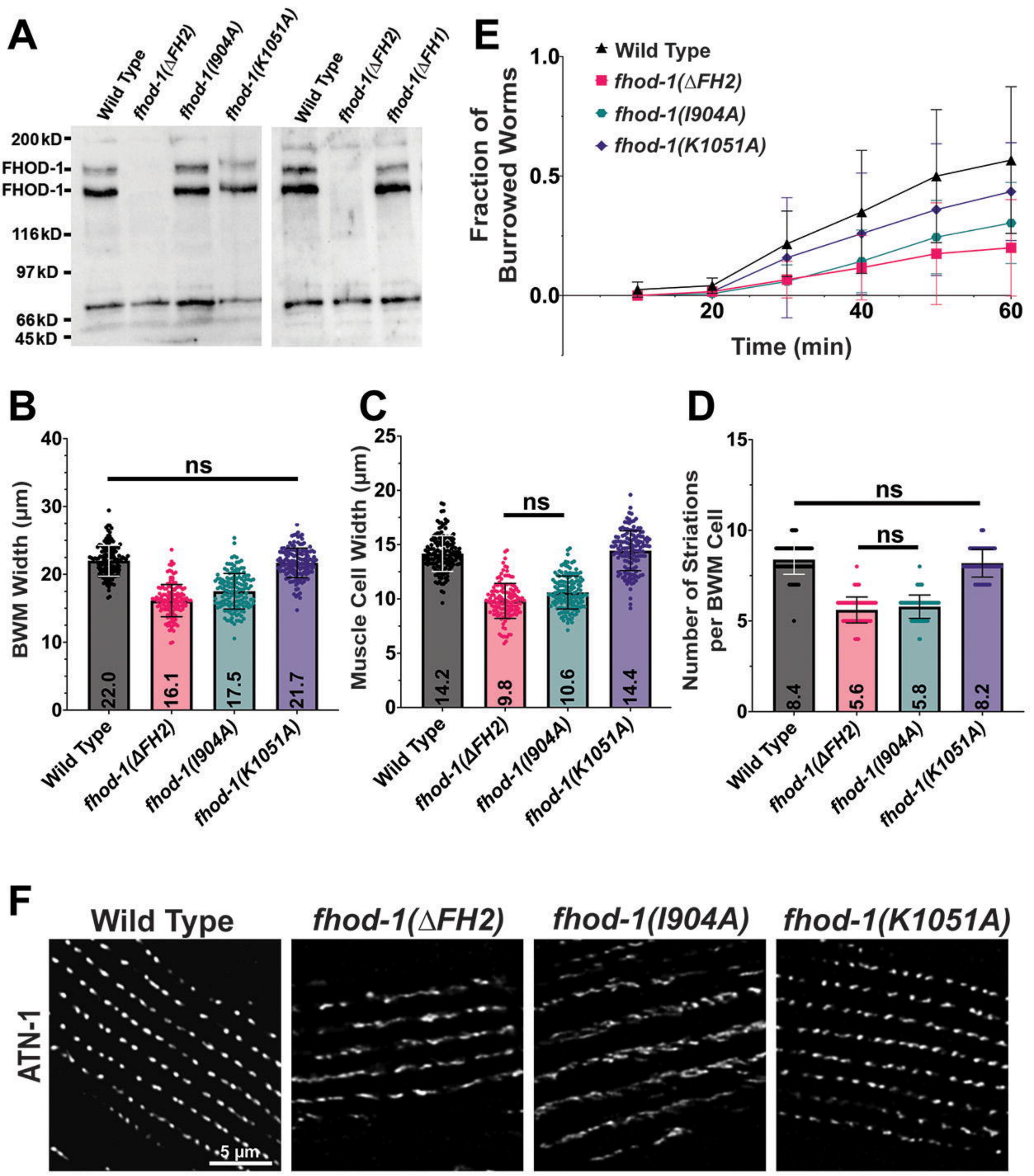
A
Wild Type
fhod-1(ΔFH2)
fhod-1(I904A)
fhod-1(K1051A)
Wild Type
fhod-1(ΔFH2)
fhod-1(ΔFH1)
200 kD
FHOD-1
FHOD-1
116 kD
97 kD
66 kD
45 kD
E
Wild Type
fhod-1(ΔFH2)
fhod-1(I904A)
fhod-1(K1051A)
Fraction of Burrowed Worms
1.0
0.5
0.0
20
40
60
Time (min)
B
BWM Width (µm)
ns
22.0
16.1
17.5
21.7
C
Muscle Cell Width (µm)
ns
14.2
9.8
10.6
14.4
D
Number of Striations per BWM Cell
ns
ns
8.4
5.6
5.8
8.2
F
Wild Type
fhod-1(ΔFH2)
fhod-1(I904A)
fhod-1(K1051A)
ATN-1
5 µm

Figure 2

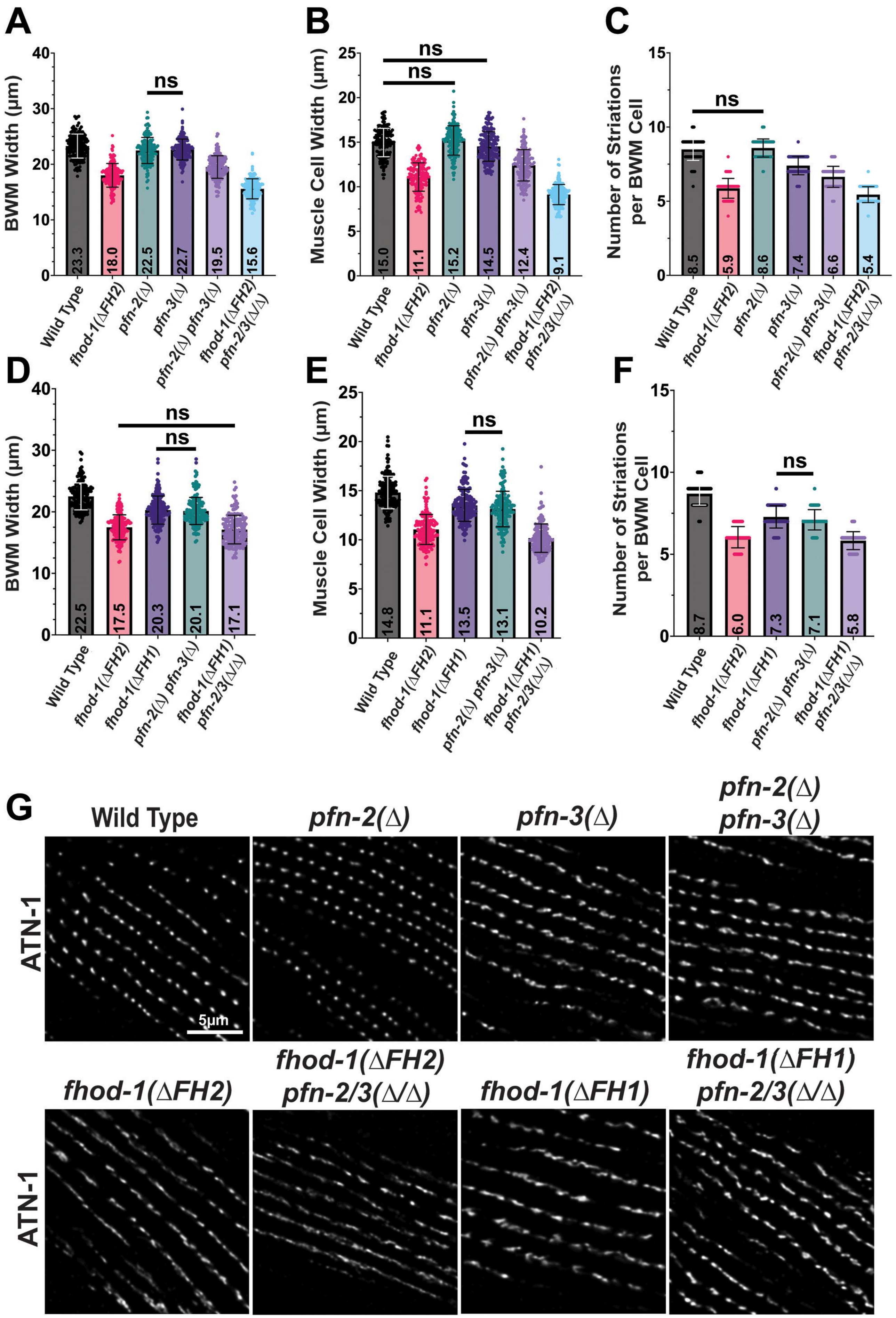
A
BWM Width (µm)
ns
23.3
18.0
22.5
22.7
19.5
15.6
Wild Type
fhod-1(ΔFH2)
pfn-2(Δ)
pfn-3(Δ)
pfn-2(Δ) pfn-3(Δ)
fhod-1(ΔFH2) pfn-2/3(Δ/Δ)
B
Muscle Cell Width (µm)
ns
ns
15.0
11.1
15.2
14.5
12.4
9.1
C
Number of Striations per BWM Cell
ns
8.5
5.9
8.6
7.4
6.6
5.4
D
BWM Width (µm)
ns
ns
22.5
17.5
20.3
20.1
17.1
Wild Type
fhod-1(ΔFH2)
fhod-1(ΔFH1)
pfn-2(Δ) pfn-3(Δ)
fhod-1(ΔFH1) pfn-2/3(Δ/Δ)
E
Muscle Cell Width (µm)
ns
14.8
11.1
13.5
13.1
10.2
F
Number of Striations per BWM Cell
ns
8.7
6.0
7.3
7.1
5.8
G
Wild Type
pfn-2(Δ)
pfn-3(Δ)
pfn-2(Δ) pfn-3(Δ)
ATN-1
5µm
fhod-1(ΔFH2)
fhod-1(ΔFH2) pfn-2/3(Δ/Δ)
fhod-1(ΔFH1)
fhod-1(ΔFH1) pfn-2/3(Δ/Δ)
ATN-1

Figure 3

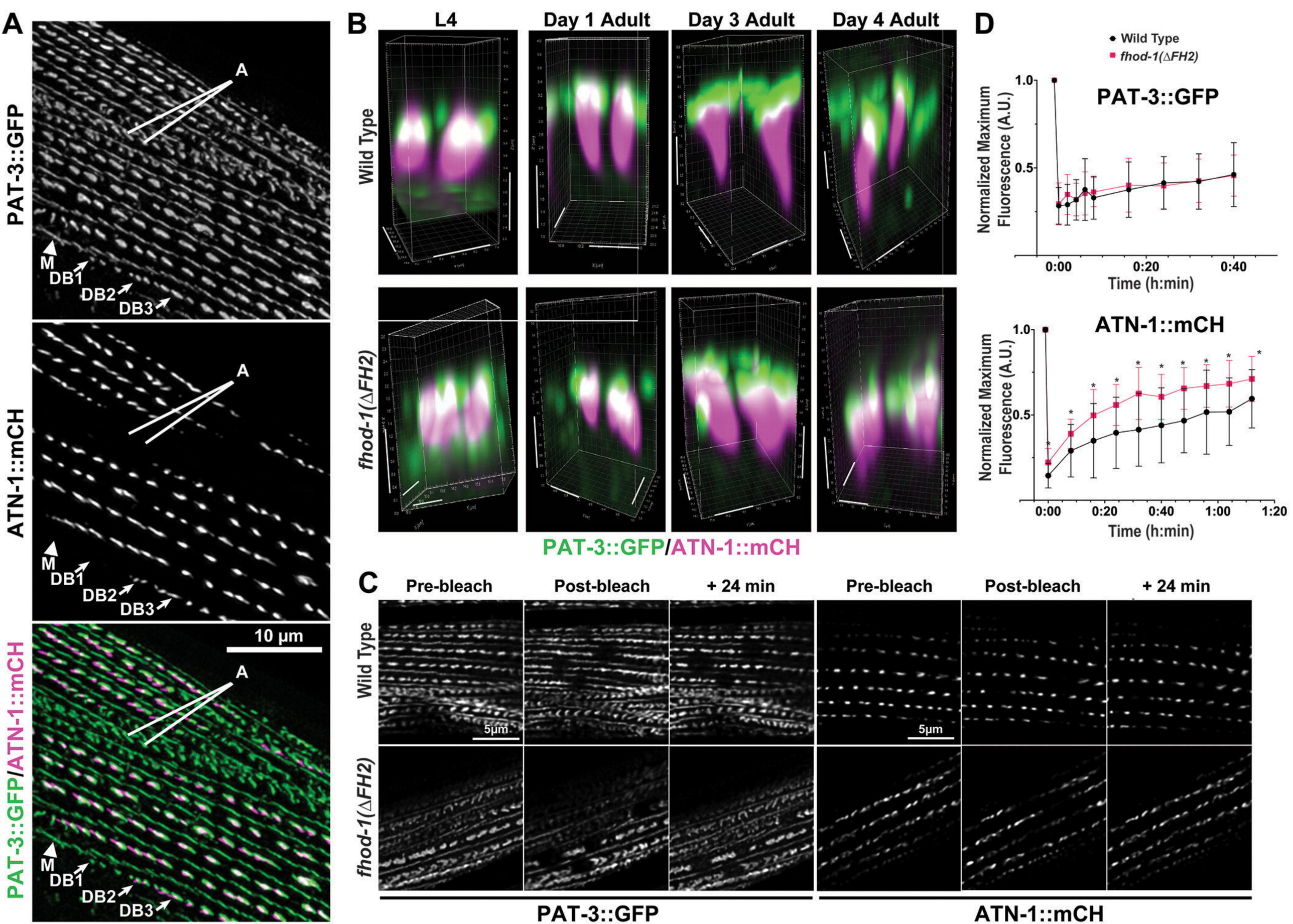
A
PAT-3::GFP
ATN-1::mCH
PAT-3::GFP/ATN-1::mCH
A
M
DB1
DB2
DB3
10 µm
B
L4
Day 1 Adult
Day 3 Adult
Day 4 Adult
Wild Type
fhod-1(ΔFH2)
PAT-3::GFP/ATN-1::mCH
C
Pre-bleach
Post-bleach
+ 24 min
Pre-bleach
Post-bleach
+ 24 min
Wild Type
fhod-1(ΔFH2)
5µm
5µm
PAT-3::GFP
ATN-1::mCH
D
Wild Type
fhod-1(ΔFH2)
PAT-3::GFP
Normalized Maximum Fluorescence (A.U.)
1.0
0.5
0:00
0:20
0:40
Time (h:min)
ATN-1::mCH
Normalized Maximum Fluorescence (A.U.)
1.0
0.5
0:00
0:20
0:40
1:00
1:20
Time (h:min)

Figure 4

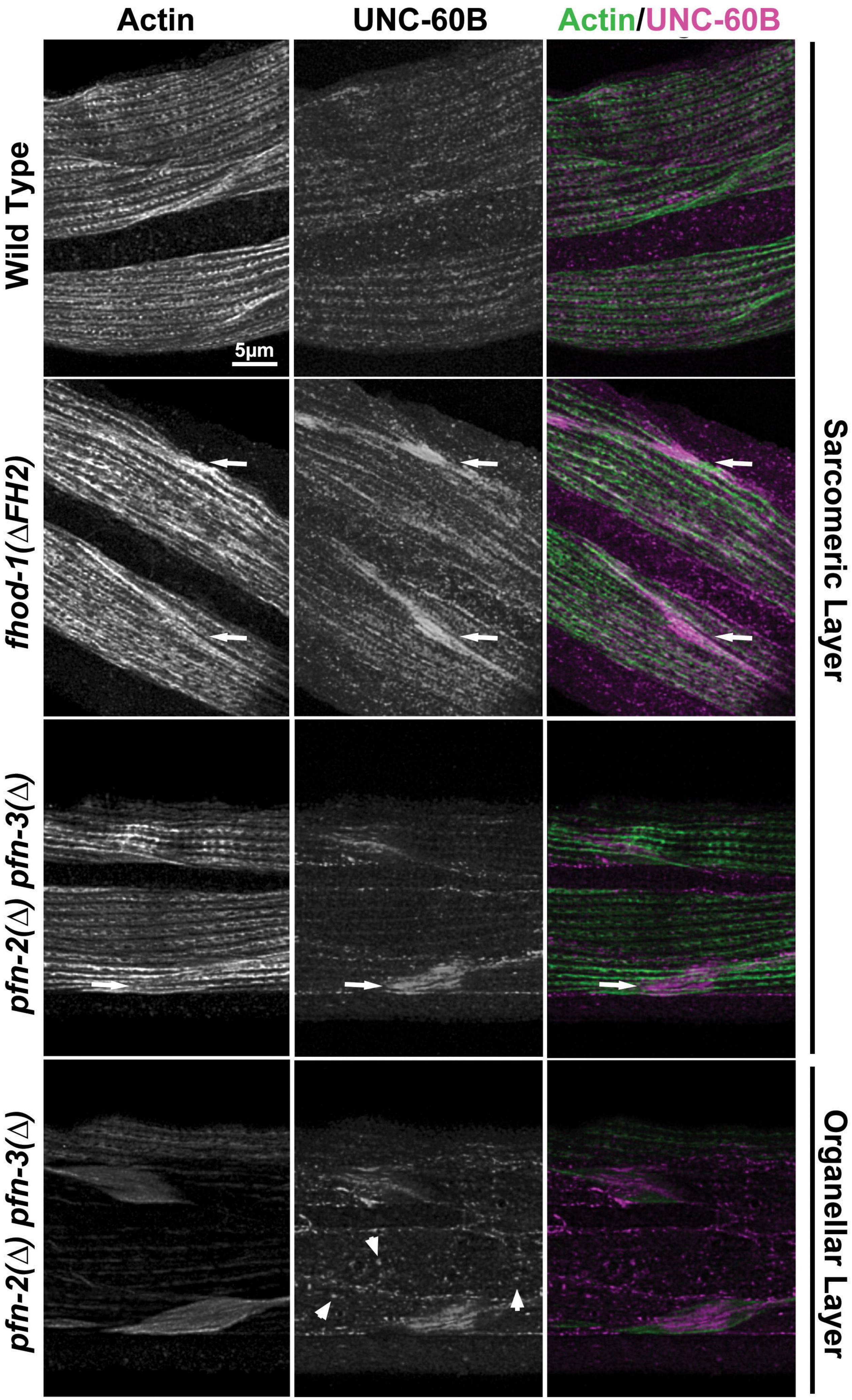
Actin
UNC-60B
Actin/UNC-60B
Wild Type
fhod-1(ΔFH2)
pfn-2(Δ) pfn-3(Δ)
pfn-2(Δ) pfn-3(Δ)
5μm
Sarcomeric Layer
Organellar Layer

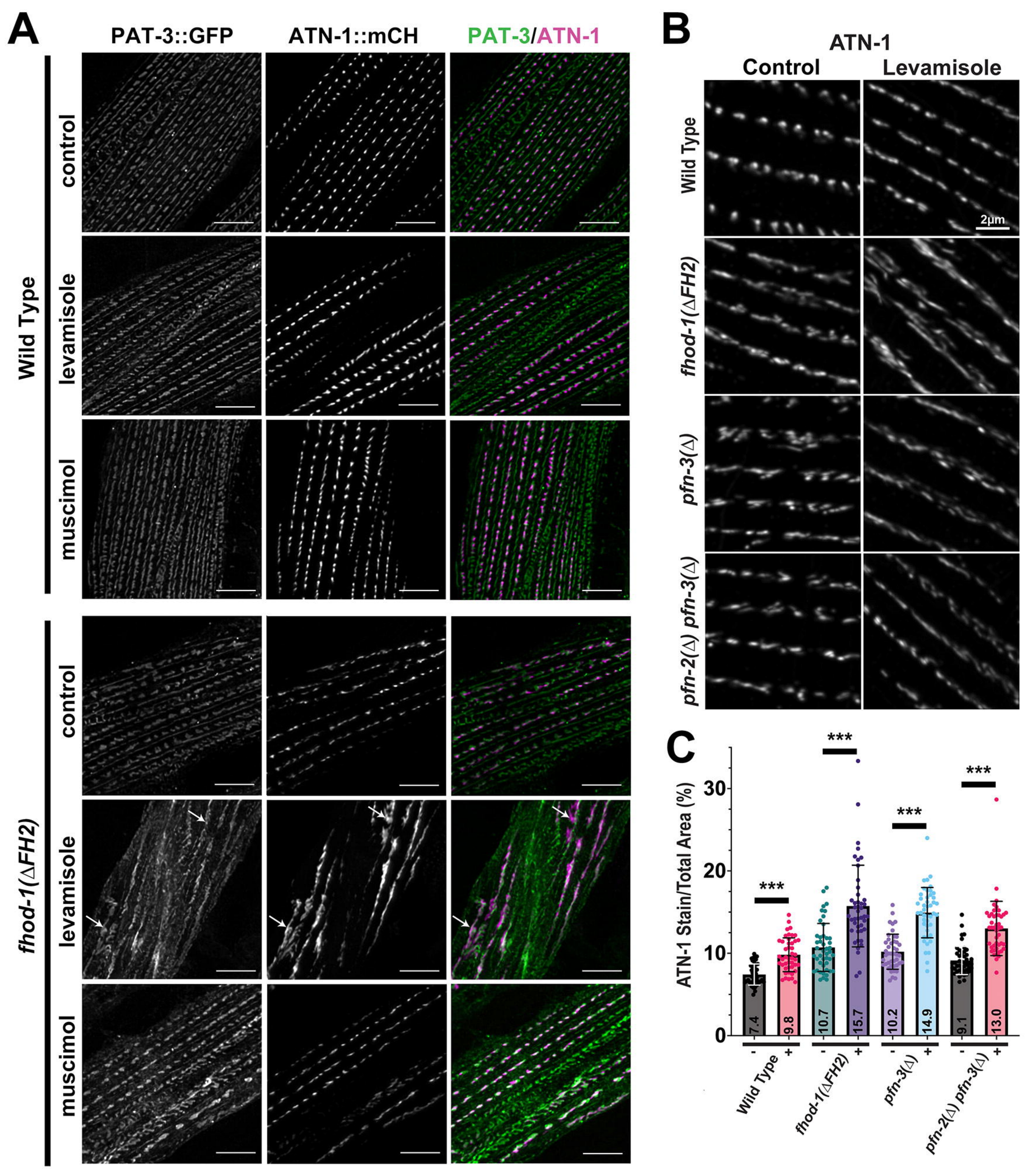
A
PAT-3::GFP
ATN-1::mCH
PAT-3/ATN-1
Wild Type
control
levamisole
muscimol
fhod-1(ΔFH2)
control
levamisole
muscimol
B
ATN-1
Control
Levamisole
Wild Type
fhod-1(ΔFH2)
pfn-3(Δ)
pfn-2(Δ) pfn-3(Δ)
2μm
C
ATN-1 Stain/Total Area (%)
0
10
20
30
***
***
***
***
7.4
9.8
10.7
15.7
10.2
14.9
9.1
13.0
-
+
Wild Type
fhod-1(ΔFH2)
pfn-3(Δ)
pfn-2(Δ) pfn-3(Δ)

Figure 6

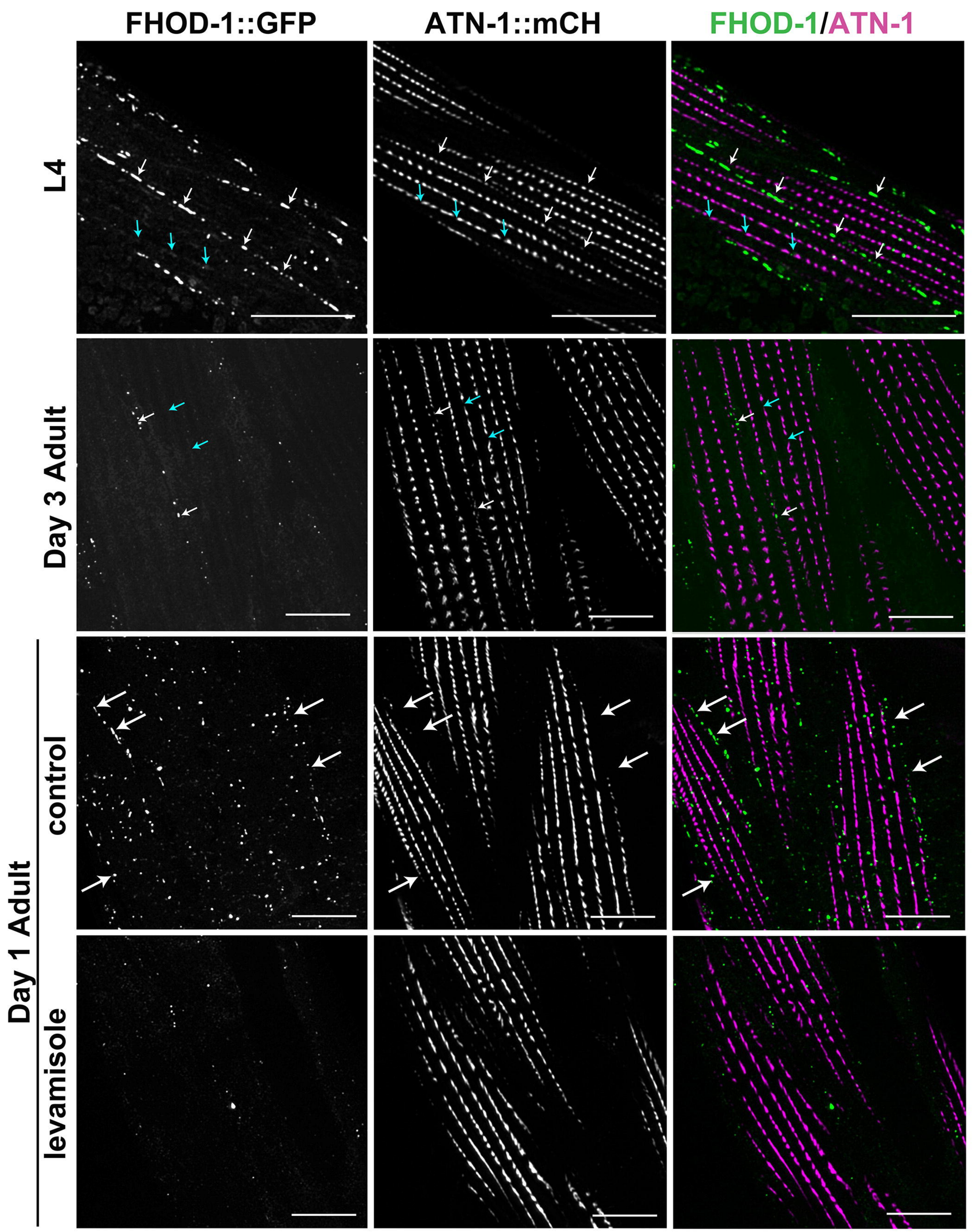
FHOD-1::GFP
ATN-1::mCH
FHOD-1/ATN-1
L4
Day 3 Adult
Day 1 Adult
control
levamisole

Figure 7